DEVELOPMENT OF HIGH PERFORMANCE SINTERED Si$_3$N$_4$

C.D. Greskovich and J.A. Palm

September 1980

GENERAL ELECTRIC CO.
CORPORATE RESEARCH AND DEVELOPMENT
SCHENECTADY, NY 12301

Final Technical Report — September 1978 — April 1980

Contract Number DAAG46-78-C-0058

Approved for public release; distribution unlimited

Prepared for
ARMY MATERIALS AND MECHANICS RESEARCH CENTER
Watertown, Massachusetts 02172

under AMMRC/DOE Interagency Agreement EC-76-A-1017-002
Department of Energy
Division of Transportation Energy Conservation
Heat Engine Highway Vehicle Systems Program

U. S. DEPARTMENT OF ENERGY

Division of Transportation Energy Conservation

CONSERVATION

DISPOSITION INSTRUCTIONS

REPORT DOCUMENTATION PAGE	READ INSTRUCTIONS BEFORE COMPLETING FORM

1. REPORT NUMBER	2. GOVT ACCESSION NO.	3. RECIPIENT'S CATALOG NUMBER
AMMRC TR 80-46		

4. TITLE (and Subtitle)	5. TYPE OF REPORT & PERIOD COVERED
Development of High Performance Sintered Si_3N_4	Final Technical Report Sept. 1978 - April 1980
	6. PERFORMING ORG. REPORT NUMBER
	SRD-80-111

7. AUTHOR(s)	8. CONTRACT OR GRANT NUMBER(s)
C.D. Greskovich and J.A. Palm	DAAG 46-78-C-0058

9. PERFORMING ORGANIZATION NAME AND ADDRESS	10. PROGRAM ELEMENT, PROJECT, TASK AREA & WORK UNIT NUMBERS
General Electric Company Corporate Research and Development Schenectady, New York 12301	

11. CONTROLLING OFFICE NAME AND ADDRESS	12. REPORT DATE
Army Materials and Mechanics Research Center Watertown, MA 02172	September 1980
	13. NUMBER OF PAGES
	79

14. MONITORING AGENCY NAME & ADDRESS(if different from Controlling Office)	15. SECURITY CLASS. (of this report)
	Unclassified
	15a. DECLASSIFICATION/DOWNGRADING SCHEDULE

16. DISTRIBUTION STATEMENT (of this Report)

Approved for public release; distribution unlimited.

17. DISTRIBUTION STATEMENT (of the abstract entered in Block 20, if different from Report)

18. SUPPLEMENTARY NOTES

19. KEY WORDS (Continue on reverse side if necessary and identify by block number)

Gas Pressure Sintering   Beryllium Silicon Nitride
Nitrogen Ceramics   Oxygen Control
Silicon Nitride   High Temperature Properties
Sintering

20. ABSTRACT (Continue on reverse side if necessary and identify by block number)

A gas pressure sintering (GPS) process has been developed to produce Si_3N_4, containing 0.5-1.0 wt% Be and 2.5-3.7 wt% O, with >99% relative density. The modulus of rupture of GPS Si_3N_4 at 1300 °C was 553 MNm^{-2} (80,200 psi), representing 93% of its room temperature strength. The creep and oxidation resistances were outstanding and evidenced by creep rates of

4.6 x 10^{-7} and 6.9 x $10^{-6} h^{-1}$ at a stress of 69 MNm^{-2} (10,000 psi) at 1300 and 1400 ^{o}C in air, respectively, and parabolic oxidation rates of 1 x 10^{-12} and 6 x 10^{-12} kg^{2} m^{-4} s^{-1} at temperatures between 1300 and 1500 ^{o}C in air. GPS Si$_3$N$_4$ survived a long term creep experiment of 207 MNm^{-2} (30,000 psi) stress for 300 h at 1305 ^{o}C in air. A post sintering anneal increased the creep resistance of GPS Si$_3$N$_4$ by a factor of 6. The fracture toughness at room temperature and thermal expansion coefficient between R.T. and 1000 ^{o}C were 2.9 MNm$^{-3/2}$ and 2.8 x 10^{-6} ^{o}C^{-1}, respectively.

The GPS process was successful in producing high density (98%), small blades of sintered Si$_3$N$_4$. Although problems with nonuniform porosity and surface microcracks were observed for the sintered blades, these problems are not intrinsic to the GPS process.

SUMMARY OF IMPORTANT RESULTS

A gas pressure sintering (GPS) process has been developed to produce sintered Si_3N_4, containing 0.5-1.0 wt% Be and 2.5-3.7 wt% O, with high relative densities and outstanding thermomechanical properties. The density of the sintered product was typically greater than 99% of the theoretical density (3.18 g/cc). The average modulus of ruptures in 3-pt bend at room temperature and $1300^{o}C$ in air were 597 MNm^{-2} (86,540 psi) and 553 MNm^{-2} (80,200 psi), respectively. The short-term strength retention at $1300^{o}C$ in air was about 93% of the room temperature strength. The Weibull modulus was 8.3 for the ten bars broken at room temperature and 12.9 for the six bars broken at $1300^{o}C$. Strength limiting flaws originated in the specimen surfaces in all cases.

The creep resistance of GPS Si_3N_4 was excellent and represented by steady-state creep rates of only 4.6×10^{-7} and 6.9×10^{-6} h^{-1} at 1300 and $1400^{o}C$, respectively, for an applied stress of 69 MNm^{-2} (10,000 psi). Post-sintering annealing permitted crystallization of some of the residual glassy phase in the sintered product and resulted in a 6-fold increase in the creep resistance. The outstanding creep resistance of GPS Si_3N_4 was further verified by a long term creep experiment in which a low creep rate of 3.3×10^{-7} h^{-1} was measured for an annealed bar exposed to a stress of 207 MNm^{-2} at $1305^{o}C$ in air for 300 h (12.5 days). The creep mechanism must be interpreted in terms of a creep stress exponent of ~ 2.1, an enthalpy of activation of ~ 600 kJ/mole and the micro-structural observations showing the formation of isolated cavities in the glassy-phase pockets at 3-grain intersections followed by interconnection of these cavities along grain faces as the total creep strain increases.

The oxidation rate of GPS Si_3N_4 was extremely low between 1000 and $1500^{o}C$ and dependent on impurity transport in the furnace atmosphere during

oxidation. Typically, the parabolic rate constants ranged between about 1×10^{-12} and 6×10^{-12} kg^2 m^{-4} s^{-1} at temperature between 1300 and 1500°C in air for times up to 160 h. A thin oxide scale of alpha cristobalite was coherently-bonded to the GPS Si_3N_4 material in all cases. There was no catastropic oxidation of GPS Si_3N_4 at 1000°C in air after ∿ 100 hours.

The fracture toughness of GPS Si_3N_4 measured by the microhardness indentation method was 2.9 $MNm^{-3/2}$ and compares with 3.7 $MNm^{-3/2}$ measured for NC-132 Si_3N_4. The Vicker's hardness number was ∿ 1650 kg/mm^2 for a load of 500 g. Finally, the thermal expansion coefficient between room temperature and 1000°C was measured as $2.8 \times 10^{-6}°C^{-1}$.

Complex shapes of modified T-700 blades were slip-cast from a processed, high surface area powder and subsequently sintered by the GPS process to average densities as high as 98% of the theoretical density. Microcracks on the surfaces of the sintered blades resulted from small tears developed during removal of the green blade from the mold. A larger amount of porosity developed in the central region of the sintered blades and is probably related to the thixotropic nature of the slip.

FOREWORD

TABLE OF CONTENTS

LIST OF ILLUSTRATIONS

ix

LIST OF TABLES

I. INTRODUCTION

Silicon nitride based materials are currently receiving a great deal of attention for potential application in automotive gas turbines operating eventually at turbine inlet temperatures of $\sim 1370^\circ C$ ($2500^\circ F$). Perhaps the most demanding ceramic part contemplated for use is the rotor, approximately 12.5 cm in diameter and capable of high strength (690 MN/m^2) to about $1000^\circ C$, good oxidation and creep resistance to about $1300^\circ C$, and having the potential for mass production into near-net-shapes. Until recently, the only two forms of Si_3N_4 available for use are reaction-bonded and hot-pressed Si_3N_4. Although reaction-bonded Si_3N_4 can be mass produced conveniently into intricate shapes and exhibit adequate creep properties, it suffers from poor oxidation behavior (because of the high residual porosity of $\sim 15\%$) and low fracture strength (typically <500 MN/m^2). Hot pressed Si_3N_4 is difficult to mass produce into complex shapes at reasonable costs and usually has poor creep behavior at T >$1200^\circ C$. Because of the inadequacies of reaction-bonded and hot-pressed forms of Si_3N_4, the development of sintered Si_3N_4 was cited as a priority goal for materials development for small automotive gas turbine engines in 1974[1]. In fact, it was in 1974 that developments in SiC[2] and Si_3N_4[3] research led to the fabrication of dense (>90% of the theoretical density) ceramics by the sintering process.

The promotion of sintering (macroscopic densification in the absence of applied pressure) is caused by the addition of sintering aids which have been identified as moderate additions (1-20 wt%) of MgO[3-6], Y_2O_3 + Al_2O_3[7], Al_2O_3 + AlN (SiAlON)[9-11], MgO + BeO[12], MgO + BeO + CeO_2[12] and CeO_2[13] in Si_3N_4. From the information available so far, liquid-phase sintering apparently dominates the densification of Si_3N_4 and gives rise to polyphase microstructures. Although scanty information is available on the high temperature mechanical properties of

1

sintered Si_3N_4, it is recognized that the long term retention of strength, creep and oxidation resistance and other time dependent properties will depend on the grain boundary (glassy) phase which is generally present. In order for sintered Si_3N_4 ceramics to meet the demanding requirements of a useful rotor in a small automotive gas turbine engine, considerable development work and feasibility testing must be pursued over a realistic time scale.

The processing of sintered Si_3N_4 ceramics useful for high performance thermomechanical applications requires careful consideration of the amount and chemical composition of the intergranular glassy phase surrounding the β-Si_3N_4 grains in the final product. It is reasonably-well established that optimum mechanical properties of dense Si_3N_4 are expected by reducing the amount of residual glassy phase and/or by adjusting the composition to increase viscosity or induce crystallization. However, the sinterability of powder compacts of silicon nitride will typically be adversely affected by reducing the amount of glassy-phase and by increasing its viscosity. To counterbalance this undesirably limited sinterability, higher temperatures may be used to enhance atomic mobility of the Si and N species so that the densification rate can be increased during sintering. This increase in sintering temperature (above 1800°C) then leads to the plaguing problem of thermal decomposition of silicon nitride (and of the glassy phase) and leads to density regression[3] and high levels of porosity in the final product. The problem of thermal decomposition of Si_3N_4 containing additives can be minimized or controlled by using increased nitrogen pressures (2-20 atm)[6,7,13].

In 1978, research work[14] in our laboratory demonstrated that excellent thermomechanical properties could be achieved for a new compostion of hot pressed Si_3N_4 containing small amounts of Be (0.5-1%) and O (3-3.2%). Essentially single-phase β-Si_3N_4 solid solution could be produced by using submicron α-Si_3N_4 powders with 7 wt% $BeSiN_2$ and 5.6 wt% SiO_2 as densification aids and hot

2

pressing at a temperature of 1780°C and a pressure of 69 MN/m^2.[15] At a temperature of 1400°C in air this single-phase, solid solution form of β-Si$_3$N$_4$ has a short term strength which is $\approx$90% of its room temperature value, and has remarkably low rates of oxidation (7 x 10^{-13} kg^{2}m^{-4}s^{-1}) and creep (7 x 10^{-10}s^{-1} at a stress of 70 MN/m^2)[16]. Because of these excellent thermomechanical properties, sintering investigations were initiated in the high Si$_3$N$_4$ - rich end of the Si-Be-N-O system under AMMRC/DOE support in 1978. It was believed that the amount of glassy phase containing Si, Be, N and O could be minimized becaused of the large solubility of Be and O in β-Si$_3$N$_4$. For example, phase equilibria studies[17] in the system Si$_3$N$_4$-SiO$_2$-BeO-Be$_3$N$_2$, shown in Fig 1, reveal that at 1780°C β-Si$_3$N$_4$ solid solutions extend in the direction of phenacite, Be$_2$SiO$_4$, which is unstable towards BeO and an SiO$_2$ - rich liquid above about 1560°C. The solid solubility of Be$_2$SiO$_4$ in β-Si$_3$N$_4$ extends up to $\sim$18 mole % (6.4 eq. % Be and 12.8 eq. % O) and results in nearly stoichiometric solid solutions of composition Si$_{3-x}$Be$_x$N$_{4-2x}$O$_{2x}$. It was also expected that the viscosity of the liquid (glassy) phase, which contains species of Si, Be, O and N when in equilibrium with β-Si$_{3-x}$Be$_x$N$_{4-2x}$O$_{2x}$, would be reasonably high and not too different than the viscosity of fused silica because both Be^{2+} and N^{3-} have tendencies to enter the SiO$_2$ - rich glassy structure and maintain a continuous network of bonded tetrahedra. For a reference point the viscosity of fused silica at temperatures between 1300 and 1400°C is between about 10^{11} and 10^{10} poise[18].

Details of our first year's development work on the sintering aspects and preliminary thermomechanical properties of sintered Si$_3$N$_4$ containing small amounts of Be and O has been presented in a Final Technical Report[19]. This report revealed that sintered Si$_3$N$_4$ containing 0.5 to 1.0 wt% beryllium could be densified to relative densities above 90% only with Si$_3$N$_4$ powders containing at least 2 wt% oxygen. Furthermore, metallic impurities, especially Ca, Mg and Fe on a 0.1 to 0.2
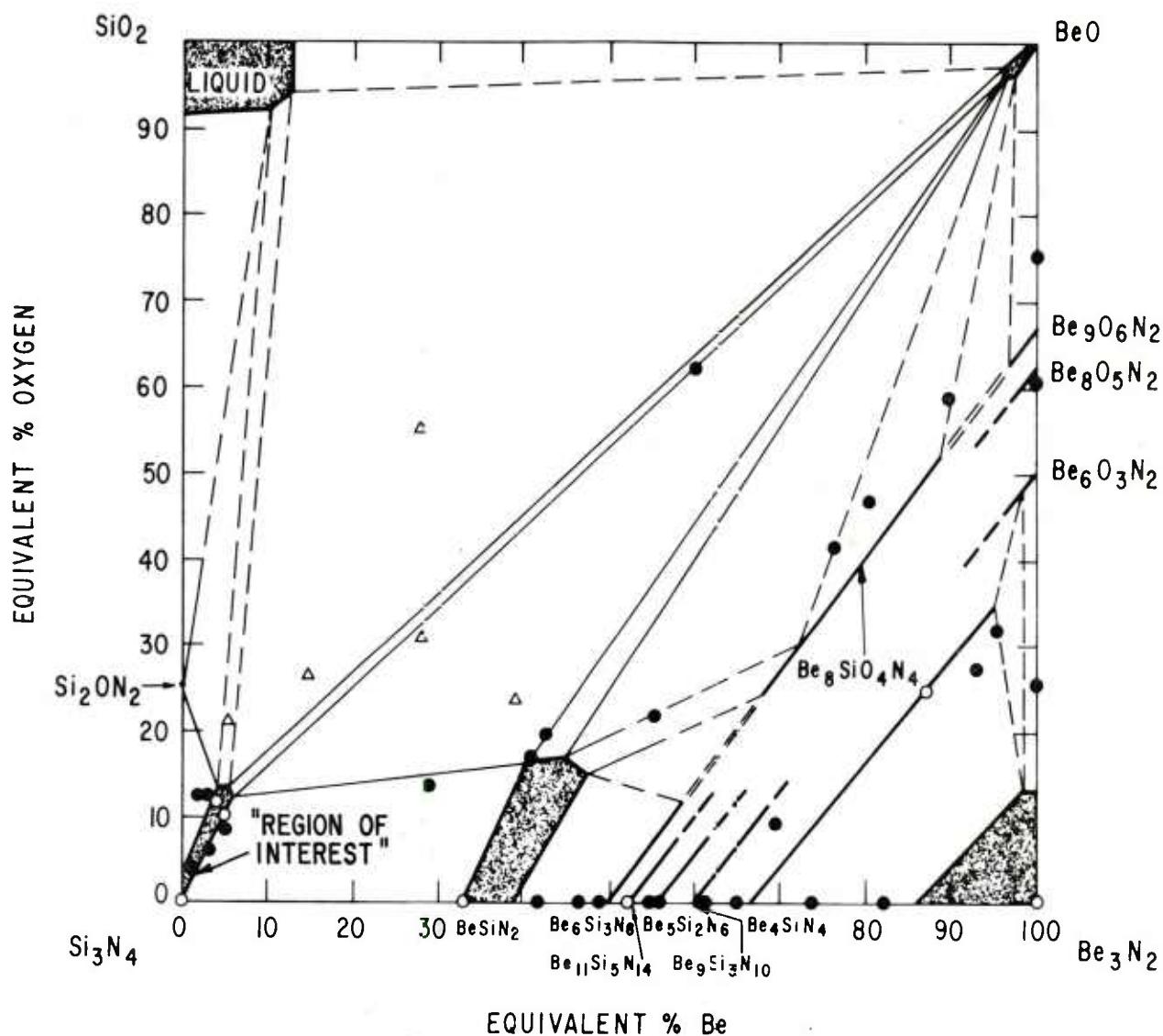
Figure 1. Isothermal section at 1780°C of the system Si_3N_4-SiO_2-BeO-Be_3N_2[17]. O=1 phase, O=2 phases, △=3 phases. The compositional region of interest is designated.

wt% level, promote sintering of beryllium-added powders. The sintering process was found to be optimized when submicron particulate compacts of the desired composition were sintered at temperatures between 2000 and 2100°C with an over-pressure (4-8 MPa) of N_2 gas. In all cases, powder compacts of Si_3N_4 were surrounded by Si_3N_4 packing powders of various quality in sintered SiC crucibles or envelopes. Sintered specimens having relative densities between 93 and 96% were only occasionally produced and provided material for the preliminary evaluation of the properties of creep and oxidation. Creep testing of two compositions carried out in the 3-point bending mode showed very low strain rates of 3×10^{-6}/h under a stress of 69 MN/m^2 at 1300°C in air, and creep (strain) rates of 3×10^{-4} and $2 \times 10^{-5}h^{-1}$ under the same stress at 1450°C. These values approached the lowest creep rates for any silicon nitride (excluding chemically vapor deposited Si_3N_4) material reported in the literature[20]. The oxidation resistance of sintered Si_3N_4 containing beryllium was found to be excellent at 1400°C in air and depended strongly on residual porosity and the level of metallic impurities in the sintered body. The oxidation rate of sintered Si_3N_4 made from high purity Si_3N_4 powder was measured as $2 \times 10^{-11} kg^2 m^{-4} s^{-1}$ at 1405°C in air and was a factor of 30 x 35 times lower than commercial hot-pressed Si_3N_4 (NC-132) which contains 1 wt% MgO as a densification aid. These preliminary results on creep and oxidation properties were highly encouraging and warranted further study in a continuation program.

II. SCOPE OF WORK

The main thrust of the current program is to provide a technological basis for the development of high performance Si_3N_4 produced by the sintering process. This program represents a continuation of the first year's effort[19] with the major objective being the reproducible fabrication of highly-dense (>98% of the theoretical value), sintered Si_3N_4 containing small amounts of Be, O and other (known)

impurities. Since high temperatures and N_2 gas pressure will be used, a gas pressure sintering process, atypical for ceramics, must be employed and understood. The interrelationships between composition, processing, microstructure and thermomechanical properties are also investigated in some detail for a high-purity starting powder of Si_3N_4. Finally, the forming of complex-shapes by slip-casting procedures and their subsequent sinterability are demonstrated.

III. FUNDAMENTAL PROBLEMS IN SINTERING Si_3N_4

There are a number of difficulties[21-23] in sintering Si_3N_4 to full density (3.18 g/cc) with excellent thermomechanical properties. Si_3N_4 is a covalently bonded solid and, consequently, a large amount of energy is required for the formation and motion of structural defects which permit diffusion of Si and N species. Since shrinkage (densification) of powder compacts of Si_3N_4 must take place by grain boundary and/or volume diffusion mechanisms, chemical additives and high temperatures are usually employed to increase the densification kinetics by increasing the effective diffusion coefficient of the rate limiting species (generally assumed to be N). In addition, submicron particle sizes are usually employed to increase the sintering kinetics as well as increase the rate of chemical reaction between the additive phases(s) and the Si_3N_4 particles. The use of micron-to-submicron powder particles is essential for uniform homogenization of all chemical ingredients and for reproducible thermomechanical properties of the final sintered products.

A liquid-phase additive that forms during sintering is typically used to speed-up the kinetics of densification. This SiO_2 - rich liquid phase permits the starting α-Si_3N_4 particles to transform into β-Si_3N_4 grains, probably via a solution-reprecipitation process, and leads to the development of a microstructure consisting of elongated β-Si_3N_4 grains intermixed with nearly equiaxed, finer β-Si_3N_4 grains. It is this type of grain structure that is characteristic of high strength

Si_3N_4 materials. However, if rapid grain growth occurs via vapor phase and/or surface diffusion processes before the liquid phase accelerates macroscopic densification, then sintered samples contain large amounts of ($\sim$10%) residual porosity. As mentioned previously, this situation is experienced as the amount of liquid phase is reduced and the viscosity (or refractoriness) increased. For optimum properties there should be little liquid phase of high viscosity in the sintered product.

High temperature mechanical properties such as creep and stress rupture are probably controlled by the same atomic mobility as the densification process by which a ceramic material is consolidated during sintering. Consequently, the higher the necessary consolidation temperature, the better is the chance to obtain a stable high temperature material during thermochemical applications. In the case of Si_3N_4, difficulties arise due to the limited thermal stability of Si_3N_4. Si_3N_4 dissociates into Si and N_2 at 1875°C and 1 atm of N_2 pressure[25]. In most sintering furnaces containing graphite components and an "unavoidable" temperature gradient, thermal decomposition and noticeable weight losses occur at temperatures above $\sim$1500°C[22]. Therefore, the development of fully-dense Si_3N_4 during sintering is a competition between the rates of densification and thermal decomposition. By using high nitrogen pressures the rate of thermal decomposition of Si_3N_4 (and liquid phases) can be suppressed and leads to the acceptance of the inconvenience of processing under high temperatures and high gas pressure, a practice heretofore unusual in ceramics.

IV. SOME THERMODYNAMIC CONSIDERATIONS

The stability of Si_3N_4 as a function of nitrogen partial pressure and temperature has been outlined in a previous report[19]. This information is presented again here for the sake of convenience and clarification of experimental results presented herein.

Silicon nitride powder decomposes at high temperatures, above about $1500^\circ C$ [22,26], into silicon and nitrogen:

$$Si_3N_4 = 3\,Si_{(1)} + 2\,N_{2(g)}; \quad \Delta G_f \tag{1}$$

If the ambient silicon vapor pressure, P_{Si}, is less than the vapor pressure above liquid silicon, silicon will evaporate and no condensed silicon appears:

$$Si_{(1)} = Si_{(v)}; \quad \Delta G_{(v)} \tag{2}$$
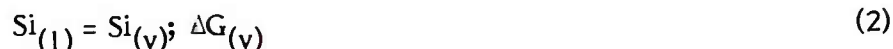
At a certain temperature the nitrogen pressure and the silicon vapor pressure are in equilibrium with Si_3N_4 and are related by equation (3).

$$P_{Si}^3 \times P_{N_2}^2 = K \tag{3}$$

where K, the equilibrium constant, is related to the sum of the free energies of reactions (1) and (2):

$$K = e - \frac{\Delta G_{(f)} + 3\,\Delta G_{(v)}}{RT} \tag{4}$$

The partial pressure of silicon at a selected temperature and nitrogen pressure can be calculated from equation (3). Using data for $\Delta G_{(f)}$ and $\Delta G_{(v)}$ from the JANAF Tables[25], P_{Si} and P_{N_2} were calculated and plotted in the diagram on Figure 2.

The set of lines from lower right to upper left are isotherms and the solid curve from lower left to upper right is the condensed Si-silicon nitride - gas coexistence boundary and depicts nitrogen pressures above which silicon nitride exists as a solid if silicon vapor is not removed from the system. It has to be emphasized that even at high nitrogen pressure Si_3N_4 will tend to decompose if silicon vapor transport out of the system is not prevented. The role of nitrogen pressure is to decrease P_{Si} such that it is below the vapor pressure in equilibrium with liquid silicon and to prevent spontaneous decomposition of Si_3N_4 into liquid silicon and nitrogen. If, for example,

Si_3N_4 is kept at 2000°C in an environment of P_{N_2} at 5 atm it will evaporate, and the rate of evaporation will be controlled either by the rate of silicon vapor transport away from the specimen or by the rate of Si_3N_4 decomposition. If, alternatively, a closed system was used, nitrogen pressure maintained at 10 atm and the temperature gradually increased, silicon vapor pressure would increase (along vertical lines in Figure 2) until the liquid-solid coexistence boundary is reached where liquid silicon forms. On further exposure all Si_3N_4 would isothermally decompose into liquid Si and N_2 and the rate of decomposition would be controlled by heat flow.

From the above discussion it follows that two conditions have to be fulfilled to prevent decomposition of Si_3N_4 at high temperatures:

(1)   Nitrogen pressure has to be sufficiently high to keep the system to the right of the solid-liquid coexistence boundary, and,

(2)   Silicon vapor loss from the system has to be prevented.

Condition (2) becomes critical at high temperatures because the rates of evaporation and vapor transport increase exponentially with temperature. One method of reducing the loss of silicon vapor over sintering compacts of Si_3N_4 is to use a buffering powder bed of Si_3N_4 in a SiC crucible open at one end. By using this method, the "region of sinterability" has been outlined in Fig. 2 for Si_3N_4 compacts containing small amounts of $BeSiN_2$ and SiO_2 as densification aids. In any sintering system, the extent of the "region of sinterability" will be affected by the degree of stagnant conditions surrounding the sintering compact, the composition and stability of the SiO_2 - rich glassy phase and impurity effects. The use of a closed BN crucible without Si_3N_4 packing powder permits lower N_2 pressures to be used at the sintering temperature during sintering of compacts of Si_3N_4 containing 7 wt% $BeSiN_2$ and 3.5 wt% oxygen, causing the region of sinterability in Fig. 2 to widen towards lower P_{N_2}.
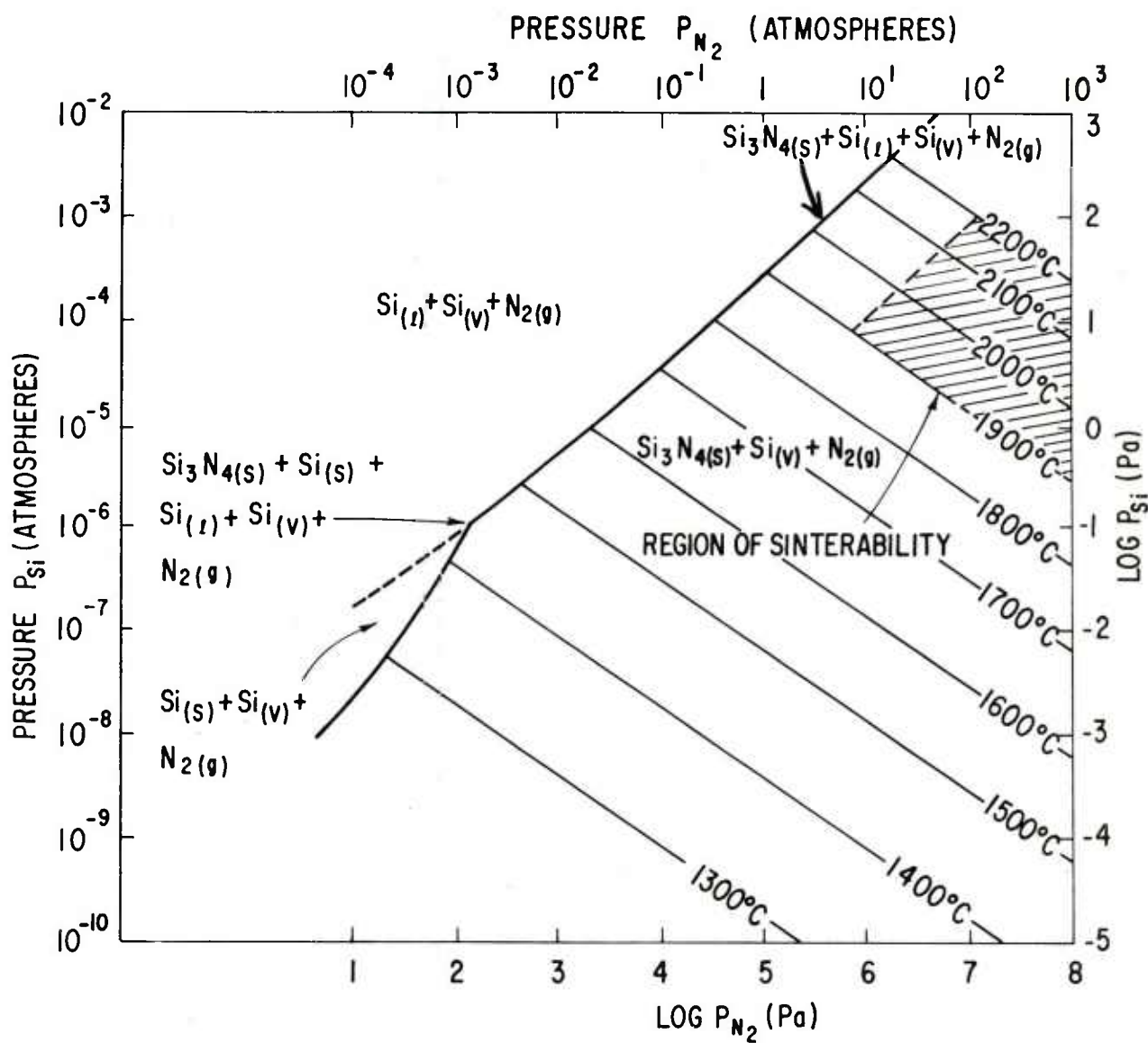
Figure 2. Silicon vapor pressure in equilibrium with silicon nitride as a function of nitrogen pressure and temperature.

In addition to control of P_{Si} over Si_3N_4 during firing in a graphite resistance furnace, there is the serious problem of thermal decomposition of the glassy phase responsible for the densification process. Since Si_3N_4, SiO_2 and the "selected" additive(s) are major reactants in the compact undergoing sintering, the following reactions are important to consider.

$$Si_3N_4(s) + 3\ SiO_2(s) \rightarrow 6\ SiO(g) + 2\ N_2(g) \tag{5}$$

$$3Si_2N_2O(s) \rightarrow Si_3N_4(s) + 3\ SiO(g) + N_2(g) \tag{6}$$

$$(Si\ M*\ ON)\ glass \rightarrow SiO(g) + N_2(g) + ? \tag{7}$$
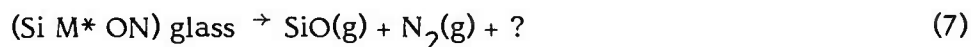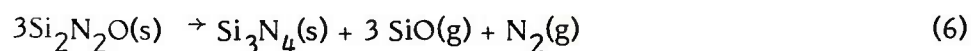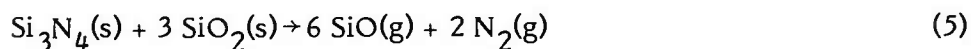
M* = metal ion in the additive phase(s)

The above reactions show clearly that the common reaction products are SiO and N_2 gases. Therefore, sintering in hyperbaric N_2 pressure will suppress these possible reactions and minimize oxygen removal from the sample via SiO gas. Reaction (5) is likely to occur in view of experiments[27] that showed that the decomposition of Si_3N_4 is accelerated by the presence of Al_2O_3, which is more stable than SiO_2. The decomposition of Si_2N_2O and "glassy" phase (reactions 6 and 7) have already been observed by the author in Si_3N_4 containing small amounts of beryllium and oxygen[15,23]. The use of a closed crucible (permeable to N_2 pressure) and high N_2 pressure is particularly advantageous for maintaining uniform distribution of the SiO_2 - rich glassy phase responsible for liquid-assisted sintering of Si_3N_4. The practical use of the forgoing theoretical considerations will be described throughout the following text.

V.   EXPERIMENTAL PROCEDURES

A.   Silicon Nitride Powders and Their Processing

There are a number of commercial suppliers of Si_3N_4 powders having various particle sizes and purity. We have procured several types of Si_3N_4

powders but worked in detail mainly with high purity powder produced by GTE Sylvania. A small number of experiments were also carried out using a standard purity (99.9%) grade of Si_3N_4, produced by H. Starck.

The as-received Sylvania powder is greater than 99.99% pure with respect to cation impurities. Optical spectroscopy results show that the concentration of Al, Fe, Ca and Mg is each less than 60 ppm. Impurity detection by energy dispersive X-ray analysis showed trace amounts of Mo and Cl. The Cl content was analyzed to be 980 ppm for one Lot of Si_3N_4 powder. Oxygen determination by neutron activation analysis revealed that one Lot of Sylvania powder had an oxygen content of 2.6 wt% whereas another Lot had 1.41 wt%. The specific surface area of both Lots of Si_3N_4 powder was between 4.5 and 5 m^2/g. Some of the powder characteristics are shown in Table I for these two powders as well as for the as-received Starck powder which contain substantial amounts of impurities of Ca, Fe and Al.

In addition to those physiochemical characteristics already mentioned, these selected Si_3N_4 powders are composed of a number of known phases. For example the GTE Sylvania powder (SN502) contains a large amount (20-40%) of amorphous Si_3N_4, and of the remaining portion that is crystalline about 92% is alpha and 8% is beta Si_3N_4. A trace of free Si can be detected in both the Sylvania and Starck Si_3N_4 powders by X-ray diffraction methods. The oxygen levels in these powders is currently believed to be associated with a thin SiO_2 film surrounding the surfaces of each Si_3N_4 particle. In the case of the Starck powder, free Si (<2 wt%) and β-SiC are secondary phases that have been detected[23]. This powder is composed primarily of crystalline Si_3N_4 phases with about 90% being of the alpha form.

The various Si_3N_4 powders were processed to reduce the average particle size to less than 0.3 μm to increase the subsequent sintering rate and

chemical reactivity with the $BeSiN_2$ additive. A selected amount of powder ($\sim$200-500 g) was ballmilled in a steel mill with steel balls and benzene for 72 h. After benzene removal by evaporation, the milled powder was acid leached in a 10% solution of HCl to remove metallic contamination acquired during prolonged milling. The suspension was repeatedly washed with H_2O until nearly Fe^{2+} free. Final sedimentation of the Si_3N_4 powder was achieved by acetone washing.

Some of the important characteristics of the milled powders are illustrated in Table I. Typically, all processed Si_3N_4 powders exhibited higher specific surface areas and oxygen contents than the starting powders. Curiously there is the general observation of an 0.06-0.07 wt% oxygen pick-up per m^2g^{-1} of new surface area produced by grinding. This oxygen uptake agrees well with our previous findings[16]. The results in Table I also show that the ball milling step can comminute Si_3N_4 particles, derived from either gas phase reaction (GTE Sylvania powder) or nitridation of Si (H. Starck powder), with little difficulty to specific surface areas of 10-15 m^2g^{-1} (corresponding average particle size of 0.19-0.13 microns, respectively). A typical photomicrograph of the final processes powder is shown if Fig. 3. The small fraction of elongated particles observed may be associated with - Si_3N_4 particles. Table I also shows that the residual Fe content in one processed powder, SN502-59, ranged between 450 and 30 ppm. This is because the Fe content could be reduced from 450 ppm to lower values either by extensive washing after HCl-leaching or by normal washing after HCL + HNO_3 leaching. It should also be pointed out that the Cl content was reduced from $\sim$980 to 500 ppm by similar processing procedures.

Other batches of powder labeled SN502-74 and SN502-87 were processed similarly as the SN502-59 batch and are not included in Table I. The

TABLE I   CHARACTERISTICS OF Si_3N_4 POWDERS

SELECTED FOR SINTERING EXPERIMENTS

Powder Origin	Internal Code	Sp. Surface area (m^2/g)	Ca (ppm)	Fe (ppm)	Al (ppm)	Cl (ppm)	Oxygen (wt%)
GTE Sylvania	SN502-23A As-received	5.0	<30	<10	<30		2.6
"	SN502-23A Processed	13.3	<40	<10			3.2
"	SN502-59[+] As-received	4.8	<60	< 100	<40	980	1.41
"	SN502-59[+] Processed	11.1	<60	450-30	200	500	1.81
H. Starck	S118 As-received	7.8	1200	700	1800		1.1
"	Stk 118 Processed	14	600	30	2100		1.47

+   Contains ~1% Be in the form of BeS_4N_2

Figure 3. Typical SEM photomicrograph of the Si_3N_4 particles of processed Sylvania powder of batch SN502-87. Mag = 5000X.

most important physiochemical characteristics of these processed powders are their specific surface area and oxygen content: $8.8 \text{ m}^2\text{g}^{-1}$ and 1.34 wt% O for processed SN502-74 powder and $10.7 \text{ m}^2\text{g}^{-1}$ and 1.85 wt% O for processed SN502-87 powder.

B.   Preparation and Processing of $BeSiN_2$

The sintering additive, $BeSiN_2$, was prepared by a method similar to that described previously[19]. Equimolar amounts of Be_3N_4 and Si_3N_4 were mixed in a plastic jar mill containing Si_3N_4 grinding medium and a sufficient amount of heptane to make a "creamy" slurry. The dried powder mixture was then placed in a SiC crucible and heated to 1750-1800°C in 2 MNm^{-2} of nitrogen pressure for 10 minutes. The resulting friable powder was examined by X-ray diffraction and found to contain primarily $BeSiN_2$ and a minor amount (<10 wt%) of β-Si_3N_4.

The $BeSiN_2$ additive has been distributed into the selected Si_3N_4 powders in two ways. In the first method, the appropriate amount of $BeSiN_2$ was mixed with processed Si_3N_4 powder via a plastic jar mill using Si_3N_4 grinding cubes and heptane as a liquid vehicle. processed powders SN502-23A and Stk 19A were treated in this manner. The second method involved adding the $BeSiN_2$ additive with the as-received Si_3N_4 powder during the initial grinding operation. This procedure offered the possibility of good chemical homogeneity of the powder mixture and optimum microstructures of the sintered product. Powder batch Sn502-59 (see Table I) and batches SN502-74 and SN502-87 contained 7 st% $BeSiN_2$ and were prepared by this method.

C.   Controlling the Oxygen Content of Si_3N_4 Powders or Compacts

During the course of this investigation and from our previous work, it was found that the oxygen content of the processed Si_3N_4 powder plays a critical role in the densification process during sintering. Generally, an

oxygen content near and above 2.5 wt% is required to promote substantial densification at $2000^{\circ}C$ of Si_3N_4 powders containing 3.5 to 7 wt% $BeSiN_2$. Consequently, the low oxygen contents of 1.81 and 1.47 wt% for SN502-59 and Stk 118 processed powders, for example, need to be increased to make use of these powders for the sintering step. Although oxygen addition to these powders can be done by the addition of colloidal silica in a liquid medium, it is difficult to avoid segregation of the SiO_2 particles during drying. Therefore, a controlled oxidation process was established which oxygenates oxygen-deficient Si_3N_4 powders to a predetermined level by control of the air oxidation treatment. The experimental work thus far centers on oxidation of several high purity powders produced by GTE Sylvania.

The experimental procedure involved oxidizing small amounts (0.5-1 g) of processed Si_3N_4 powders at various times and temperatures using Al_2O_3 crucibles. The maximum temperature of oxidation was $1000^{\circ}C$. The most reliable method of measuring a constant weight of the submicron Si_3N_4 powders both before and after an oxidation treatment was to first "condition" the Si_3N_4 powder in N_2 at $1000^{\circ}C$ for 1 h, then let the powder stand in ambient conditions for 1 h before weighing, and finally after oxidizing the powder in air the oxidized powder is allowed to stand in the same ambient conditions for 1 h before weighing. Based on the weight grain measurements, the corresponding theoretical oxygen content can be calculated from the chemical reaction between Si_3N_4 and oxygen to produce SiO_2.

$$Si_3N_4(s) + 3\,O_2(g) \rightarrow 3\,SiO_2(s) + 2\,N_2(g). \tag{8}$$
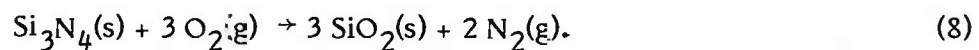
Thus, for a moderately pure Si_3N_4 powder the theoretical amount oxygen of pick-up, O_{PU}, during passive oxidation is defined as

$$O_{PU} = \frac{2\,M_o}{M_{SiO_2}} \cdot \frac{1}{1 - \dfrac{M_{Si_3N_4}}{3\,M_{SiO_2}}} \cdot \frac{\Delta W}{W_f}, \tag{9}$$

16

where M_o, M_{SiO_2} and $M_{Si_3N_4}$ are the molecular weights of oxygen, silica and silicon nitride, respectively, and $\Delta W/W_f$ is the relative weight gain after a given oxidation treatment. The substitution of the known molecular weights into Eg. (9) gives a simple relationship between O_{pu} and $\Delta W/W_f$.

$$O_{pu} = 2.4 \; \Delta W/W_f \tag{10}$$

If the initial oxygen content of the starting powder is O_i, then the total oxygen content, O_T, of an oxidized powder is given by

$$O_T = O_i + 2.4 \; \Delta W/W_f \tag{11}$$

The predicted oxygen contents of oxidized Si_3N_4 powders was then compared to the measured oxygen content determined by neutron activation analysis.

The results are presented in Table II and Figs. 4 and 5. Figure 4 clearly shows that the weight gain and the corresponding O-content of the Si_3N_4 powder increases with increasing time of oxidation at $1000^\circ C$. The oxidation kinetics follow approximately parabolic behavior with as much as 3.5 wt% oxygen acquired after 5 hr. In Fig. 5 the measured O_T as a function of weight gain is plotted as open circles for the data points in Fig. 4. These data points were found to fit remarkably well with the theoretical curve derived from Equation (11), and the resulting curve is parallel to the theoretical curve (dashed) with O_i = O. The vertical displacement of these two lines of equal slope of 2.4 is just the O_i of the starting Si_3N_4 powder. The triangles in Fig. 5 are data points for the same powder obtained in another series of oxidation experiments with the designated times and temperatures. Again, these data points fit the experimentally developed curve quite well. Figure 5 also presents some data (squares) obtained on a similarly processed powder (SN502-23A) having a much higher initial oxygen content of 3.21 wt%. The results show that the data points approximate a

17

TABLE II. OXIDATION OF PROCESSED SN502 Si$_3$N$_4$ POWDER WITH CORRESPONDING WEIGHT GAINS, OXYGEN CONTENTS AND SURFACE AREA

Powder Sample No.	Oxidation Time At 1000°C in Air (hrs)	% weight Gain	% Oxygen Content[+]	%Oxygen Pick-up	Surface Area (m^2/g)
(1)	0	0	1.81	0	11.1
(2)	0.25	0.395	3.03	1.22	8.1
(3)	1.00	0.855	4.05	2.24	7.8
(4)	3.00	1.367	4.62	2.81	7.6
(5)	5.00	1.533	5.28	3.47	7.5

[+]Total oxygen content measured by neutron activation analysis.
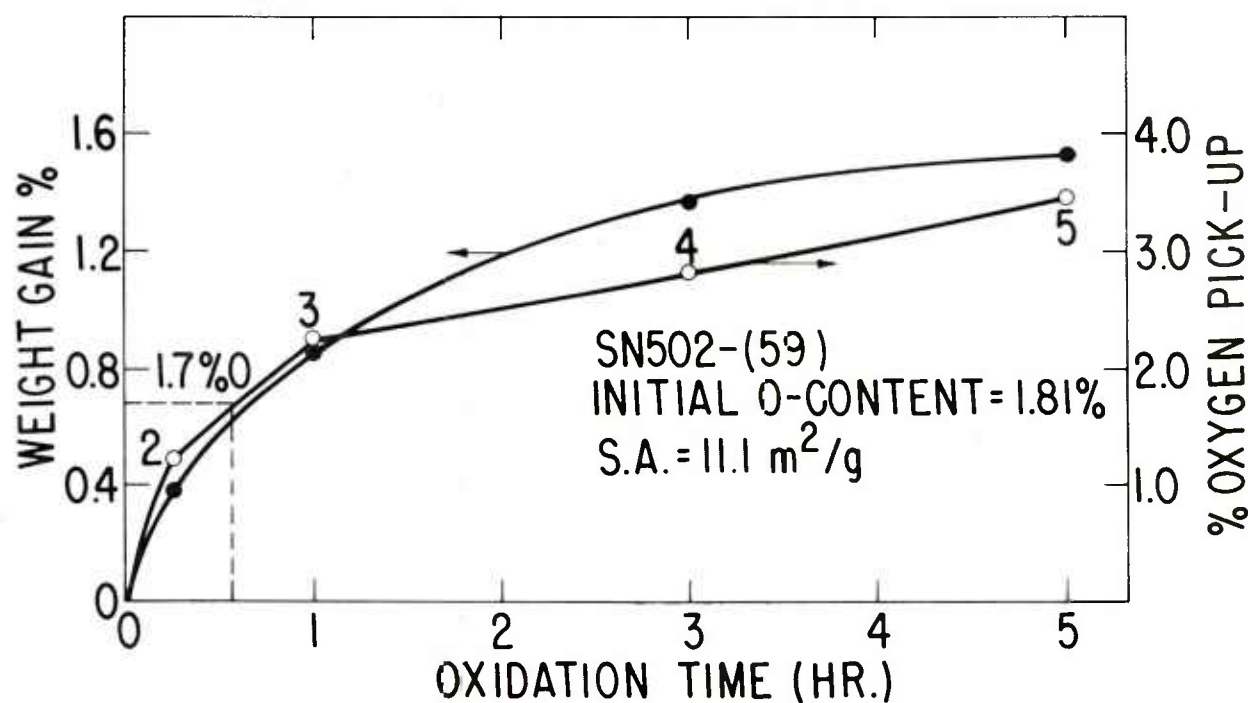
Figure 4. The percentages of weight gain and oxygen pick-up as a function of oxidation time at 1000°C in air for SN502-59 processed Si$_3$N$_4$ powder. Oxygen contents were determined by neutron activation analysis.
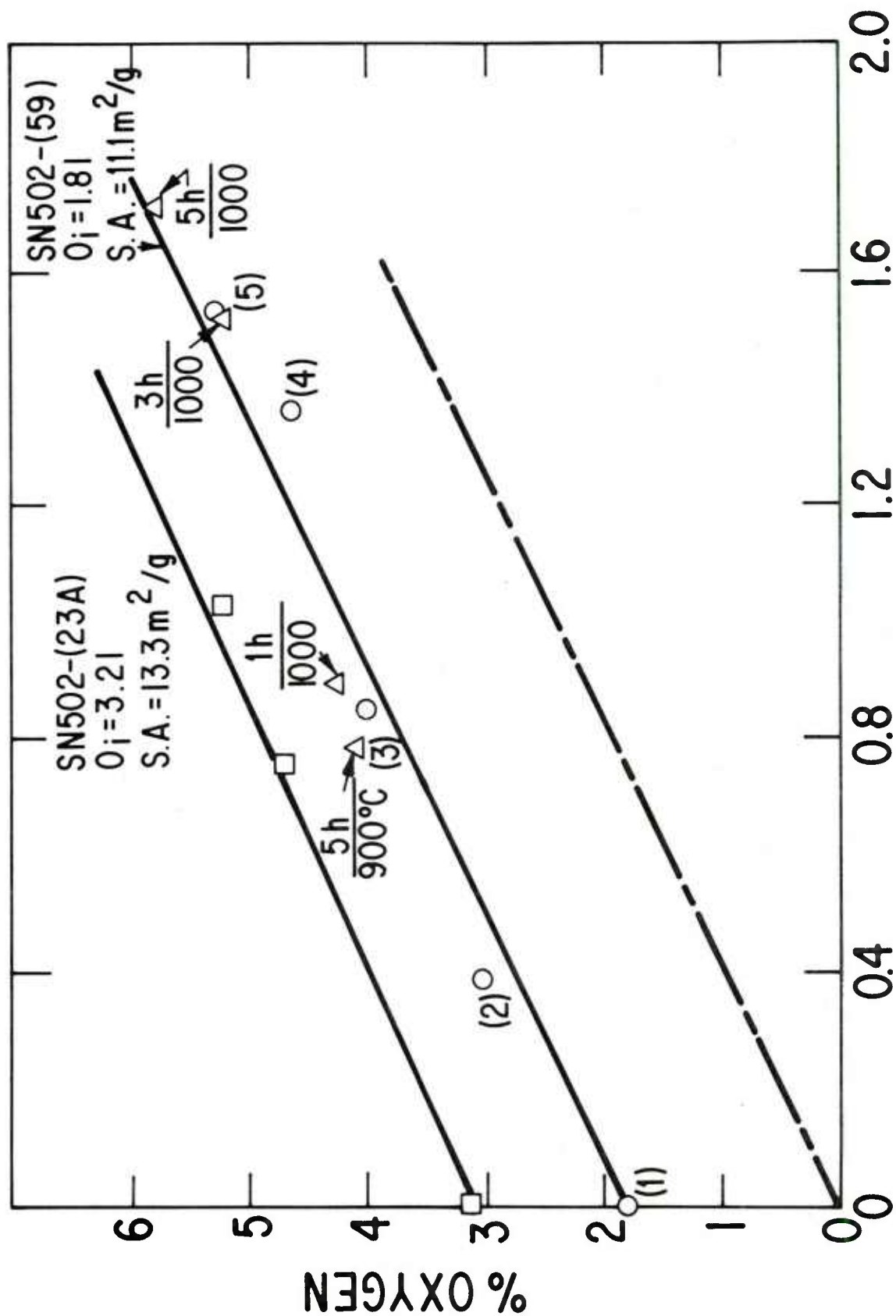
Figure 5. Percent oxygen versus percent weight gain for processed Si_3N_4 powders after oxidation in air at $1000^\circ C$. Dashed curve is the theoretical values predicted for oxygen pick-up according to Eg. (10).

straight line described also by Equation (11). Therefore, the final oxygen content O_T, of an oxidized Si_3N_4 powder cf high surface area can be measured to within ± 0.2 wt% by measuring the weight gain during oxidation in air, and this method appears to be independent of the surface area and initial oxygen content cf the starting Si_3N_4 powder.

The information generated in Figs. 4 and 5 was used to predetermine the amount of oxygen expected to be present in a large batch ($\sim$200 g) of SN502-59 Si_3N_4 powder. Since the O_i was 1.81 wt%, the kinetics of oxidation in Fig. 4 show that to increase the O_T, to $\sim$3.5 wt%, the batch should be oxidized for 30 min at 1000°C in air to pickup $\sim$1.7 wt% O. During the 30 min. oxidation test the thermal diffusivity of this large batch of Si_3N_4 powder was sufficiently low after plunging into the furnace that 10 min was required to attain the peak temperature cf 1000°C. Consequently, the effective oxidation time was only 20 min. The measured oxygen content of the oxidized powder was found to be 3.02 wt%, about 0.5 wt% lower than that originally desired, but it compares well with the predicted oxygen content of 3.15 wt% deduced from the % weight gain curve in Fig. 4 for an oxidation treatment of 20 min. This result, in addition to many measurements of weight gain performed on thick and thin powder compacts after oxidation under similar conditions, reveals that O_T of thick samples is significantly smaller than that for thin samples. The apparent sample-size effect appears to be related only to the reduced thermal diffusivity of large compacts or powder beds plunged into the hot furnace. Moderate heating rates of $\sim$10-20°C/min. to low-intermediate temperatures (850-950°C) of oxidation should minimize any size effect.

In summary, good control and distribution of the oxygen content of high purity Si_3N_4 powders can be achieved by a simple oxidation technique, in

which the theoretical prediction of oxygen content based on weight gain measurements agrees well with that measured experimentally. This technique has also been applied successfully to the oxidation of Si_3N_4 powders having total impurity levels of Ca, Mg, Al, and Fe < 1% (Starck powder), and offers an inexpensive method of determining the oxygen content to within $\pm$ 0.2 wt% for a treated powder. The uniform distribution of liquid phase in sintered compacts supports the deduction of uniform distribution of SiO_2 in the powder during oxidation. Finally, chemical analysis shows the oxidation treatment has an additional advantage of lowering the concentration of Cl to about 100–200 ppm.

D. Preparation of Si_3N_4 Powder Compacts

Powder compacts having relative green densities of 47–53% were usually made from 1 and 2.6 g of processed Sylvania Si_3N_4 powder containing a certain amount of $BeSiN_2$ additive. Under similar conditions the density of green compacts made from processed Starck powder was 60%. Several attempts were made to improve the pressing behavior of the powders by the addition of 0.5–1.0 wt% of paraffin, polyvinyl alcohol, polyethylene glycol, etc. However, little improvement in green density was realized. The final dimensions of the green compacts were usually ∿0.9 cm diameter x 0.9 cm thick for 1 g samples, and 1.5 cm diameter x 0.95 cm thick for 2.6 g samples. These compacts were first pressed in a double acting steel die at a pressure of 35 MN/m^2 followed by isostatic pressing at 200 MN/m^2. Several large green compacts weighing 14 g and with dimensions of 1.9 cm diameter x 3.3 cm long were also double pressed similarly to that described above so that mechanical test bars could be cut from the sintered billet.

As discussed in the previous section, it was necessary to oxidize a particular Si_3N_4 composition to improve its sintering behavior. This may be

achieved in one of two ways. The powder may be oxidized to a certain oxygen level or alternatively the formed powder compact may be oxidized. Experience thus far shows that more "pressing" problems occur and lower green density compacts result with an oxidized Si_3N_4 powder. Hence, if it is desirable to increase the oxygen content of a certain Si_3N_4 powder, then it may be best to oxidize the formed compact.

E.   The Sintering Procedure

A high pressure-high temperature sintering furnace designed and built in this laboratory was used for all experiments and shown in Fig. 6. Briefly, this furnace is electrically-heated via graphite foil and capable of operating up to 2300°C at 100 atm of inert gas pressure. The dimensions of the hot zone are 2.5 cm in diameter by 5 cm long. However, the formation of SiC on the graphite heater over long periods of time due to SiO and Si vapors evolved from the Si_3N_4 compacts results in hot spots and temperature gradients in the "hot zone". Nevertheless, a hot zone of 2.5 cm in length usually existed for 30 sintering runs.

One of the key features of this furnace is the ability to measure temperature reproducibly via a dense SiC tube having a closed end located in the hot zone. An optical pyrometer is focused through a glass prism and window onto the inside of the closed end of the SiC tube within which there is one atmosphere of gas pressure (right side of Fig. 6). A controller-programmer permits selection of single heating and cooling rates. The furnace shell and front and rear cooling blocks are water cooled.

A typical sintering run involves (1) placing the Si_3N_4 powder compact (previously oxidized near 1000°C to remove organic binders and to optimize the SiO_2 content) in a BN crucible with a screw-on lid, (2) evacuate the system up to 1000°C or back-fill with N_2 and pressurize while heating to

22

1000°C, (3) pressurize with nitrogen to the desired pressure, (4) continue heating at a selected heating rate while the P_{N_2} is controlled by a pressure release valve, (5) hold at the soak temperature for the desired time, (6) modify the soak temperature and/or P_{N_2} as desired, (7) cool the sintered specimen to room temperature at a predetermined rate, (8) depressurize the system and (9) remove the sintered sample from the furnace.

Temperature-pressure-time profiles for a conveniently-used thermal/ pressure cycle is presented diagramatically in Fig. 7. In this case a compact is sintered at 2000°C for 15 min. in 20 atm. of N_2 pressure followed by a 15 min. hold at 1900°C in 70 atm. of N_2 pressure.

F.   Characterization of Sintered Material

The weight loss, diametral and longitudinal shrinkages of right circular cylindrical compacts and density by the Archimedes method were routinely measured on all sintered specimens. X-ray diffraction analysis was used to determine the phases present and solid solution effects in selected sintered specimens. Energy dispersive X-ray analysis was employed to detect trace impurities. Polished sections by standard ceramographic techniques were used to reveal the size and distribution of the phases present, including the porosity. Polished sections were occasionally chemically etched in hot (180°C) caustic solution of LiOH:NaOH:KOH (1:4:4 by weight) for ∿10-20 min. to reveal the grain boundaries so that the average grain size could be determined from subsequent optical or scanning electron microscopy photo-micrographs. The fracture mode of dense (>99%), sintered Si_3N_4 was also observed by SEM. Transmission electron microscopy was used to observe small or thin intergranular phases, including voids and microcracks. In this case samples of sintered material were hand ground from ∿0.05 cm to a thickness of ∿45μm, followed by thinning to electron transparency by Ar ion

23
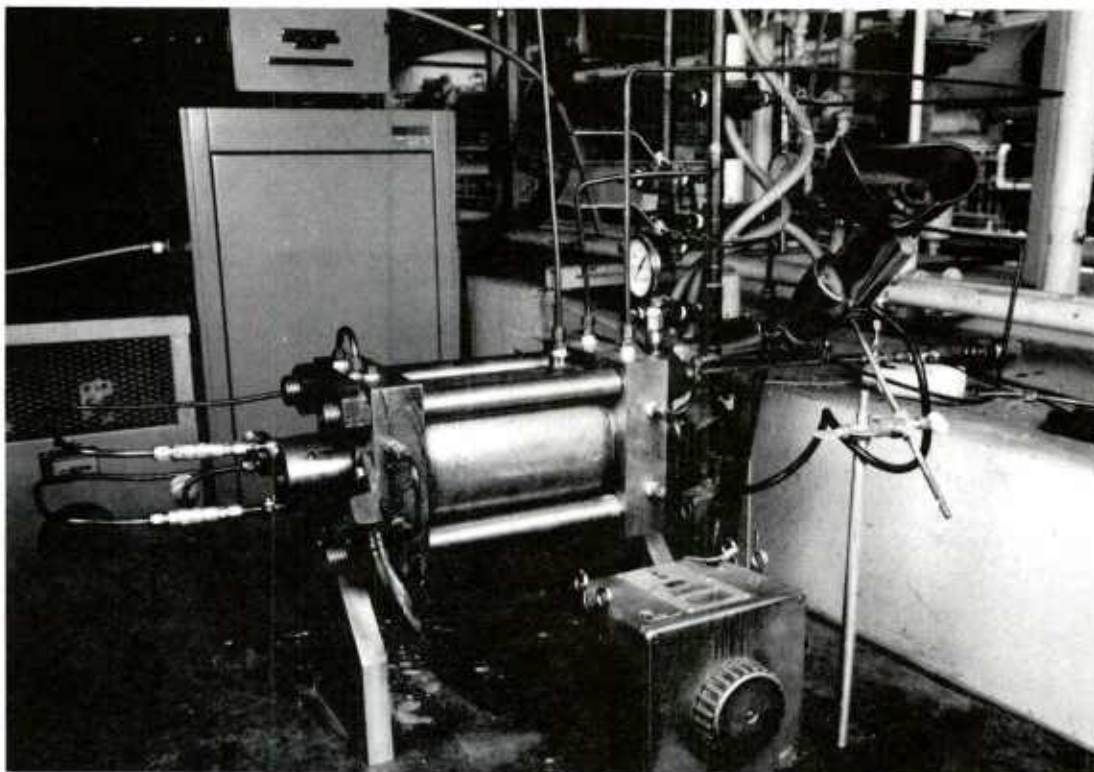
Figure 6. Sintering furnace for firing silicon nitride at high temperatures (2000-2100°C) and N_2 pressures up to 100 atom. Mag. = 1/7 X.
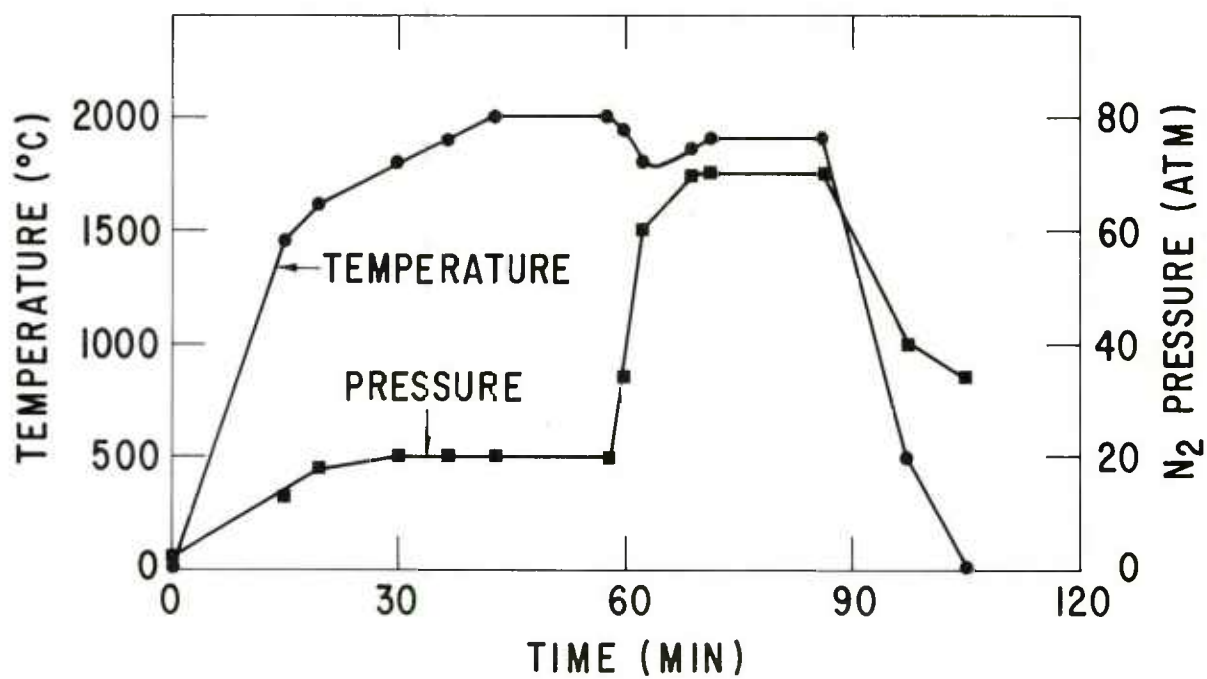
Figure 7. A typical temperature-pressure-time profile used during the sintering of silicon nitride.

beams for ~20 h. The ion-thinned specimen was placed in a double tilt specimen holder and viewed with a Siemens Elmiskop 101 using an accelerating voltage of 125 kV.

A few sintered samples of high density were analyzed chemically for their berylluim content by atomic absorption and oxygen content by neutron activation analysis.

VI. RESULTS AND DISCUSSION

A. Sintering Behavior and Characterization of Samples Sintered in a Constant p_{N_2}

In general, Si_3N_4 powder compacts containing ~1 wt% Be and 3-3.7 wt% O can be sintered to densities as high as ~93.5% of the theoretical density (~3.18 g/cc) by using nitrogen pressures (P_{N_2}) between 2.1 and 7.1 MN/m^2 (20 and 70 atm) and temperatures ranging between about 1950 and 2050°C for a time of 15 min. For compacts prepared from SN502-23A processed powder, the average linear shrinkage and weight loss of a typical sample sintered to a relative density of ~92% were 17.7% and 0.8 wt%, respectively. Weight losses were generally ~1 wt% for samples sintered for 15 min. in this range of P_{N_2} and T. However, temperatures higher than 2100°C typically resulted is some degree of thermal decomposition and density regression below ~93%, depending on the P_{N_2}. A lower temperature of 2000°C also results in samples that undergo significant thermal decomposition if the P_{N_2} is $\lesssim$ 1.2 MN/m^2 (11.7 atm). The latter phenomenon is illustrated clearly in Fig. 8 where large spheres of Si appear on the sample surface. Typically, a large weight loss $\gtrsim$ 3% occurs in Si_3N_4 samples undergoing appreciable decomposition into Si and N_2 gas.

The sintering behavior of 1 g compacts of SN502-23A processed powder was studied at temperatures between 1800 and 2050°C and nitrogen pressures between 2.1 and 7.1 MN/m^2 for a constant heating rate of $\sim$8°C/min and sintering time of 15 min. The results, illustrated in Fig. 9 show that at a P_{N_2} = 7.1 MN/m^2 there is a large effect of sintering temperature on relative density in the temperature range 1800-1975°C. The relative density increases from $\sim$60% at 1800°C to $\sim$93% at 1950°C when sintering in a P_{N_2} = 7.1 MN/m^2. Surprisingly, the relative density then drops slowly from $\sim$93% at 1950°C to 89% at 2050°C. Similar results are obtained for heating rates between 6 and 18°C/min. By decreasing the P_{N_2} from 7.1 to 2.1 MN/m^2, the relative density at about 2000°C increases from $\sim$90% to 93.5%. Consequently, the drop in density between 1950 and 2050°C appears to be less pronounced as the nitrogen pressure is reduced. The weight losses of specimens sintered between 1950 and 2050°C in the various N_2 atmospheres are nearly the same and range between 0.7 and 0.9 wt%.

The kinetics of densification for the same powder composition was then studied at 1975°C in 7.1 MN/m^2 of nitrogen pressure (see Fig. 10). There was a marked increase in relative density from 85 to 93.4% by increasing the sintering time from 3 to 8 minutes at 1975°C. However the density decreased slowly for longer times at this temperature. The density maximum of $\sim$93% occurs near the closed pore stage in the sintering compact, as evidenced by no water absorption for specimens sintered for $\geq$ 8 minutes. This effect was independent of specimen size between 1 and 2.6 g in weight.
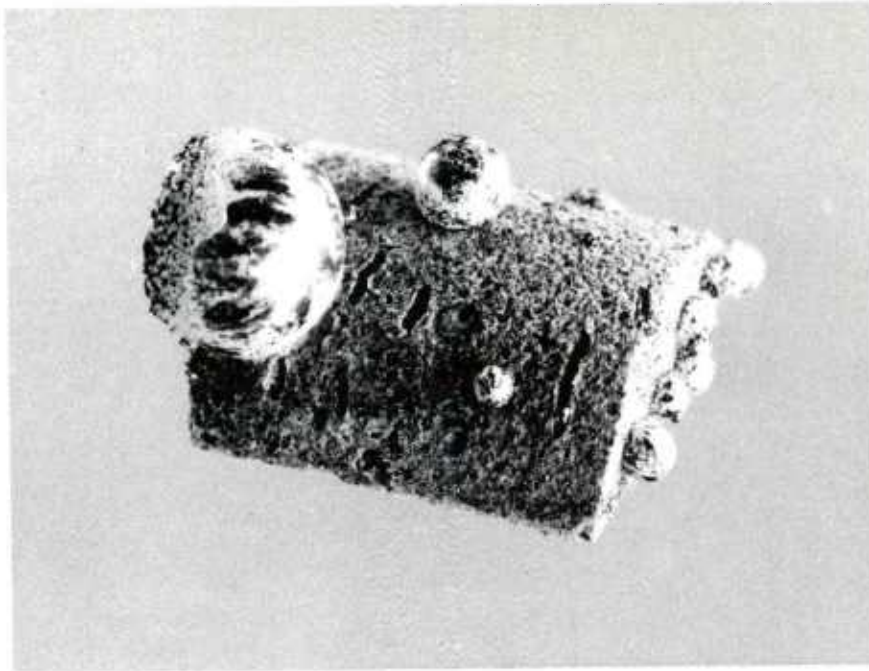
Figure 8. The formation of liquid silicon drops on silicon nitride undergoing substantial thermal decomposition during sintering. Mag. = 8 X.
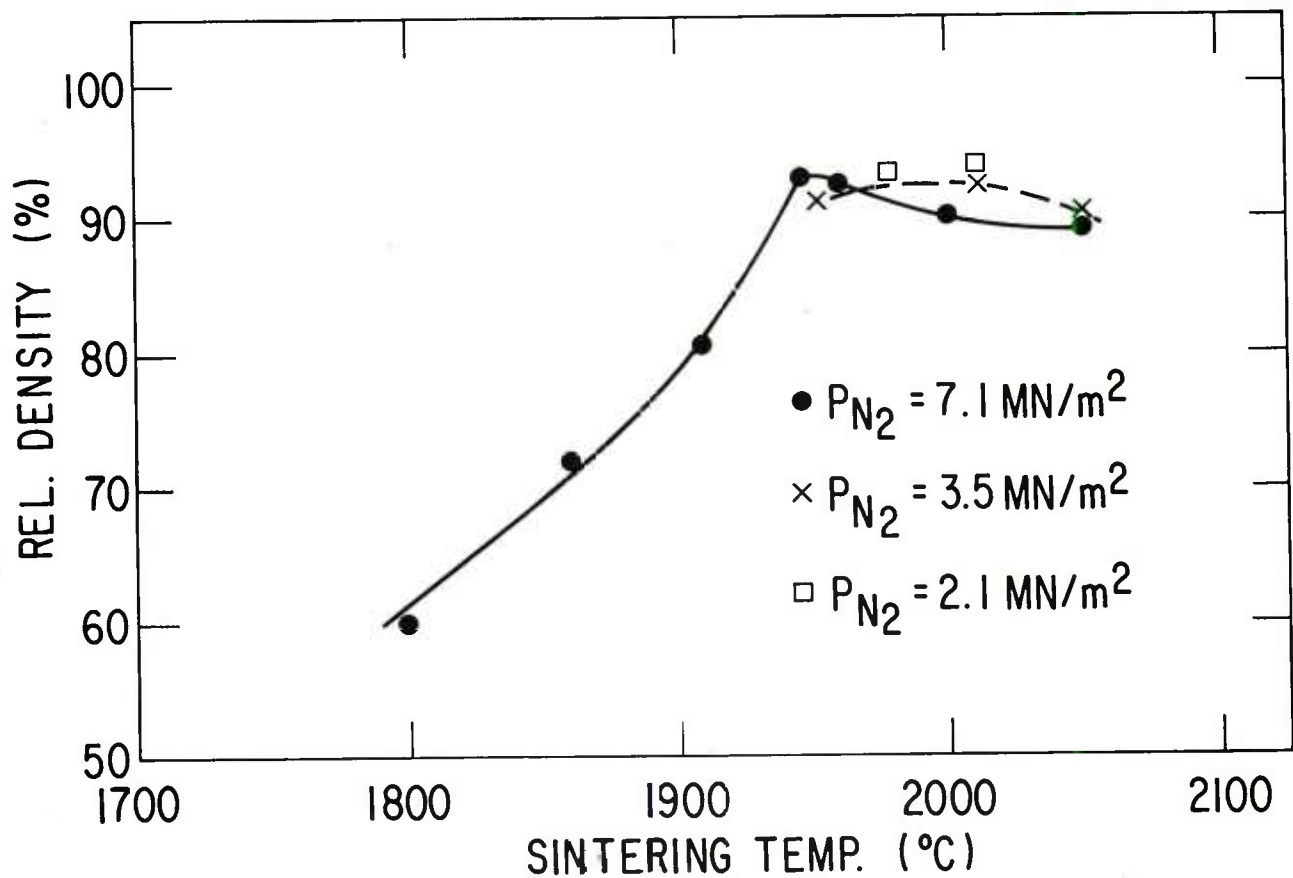

Figure 9. Relative density versus temperature for compacts of SN502-23A processed powder sintered for 15 min. in the specified N_2 pressure.
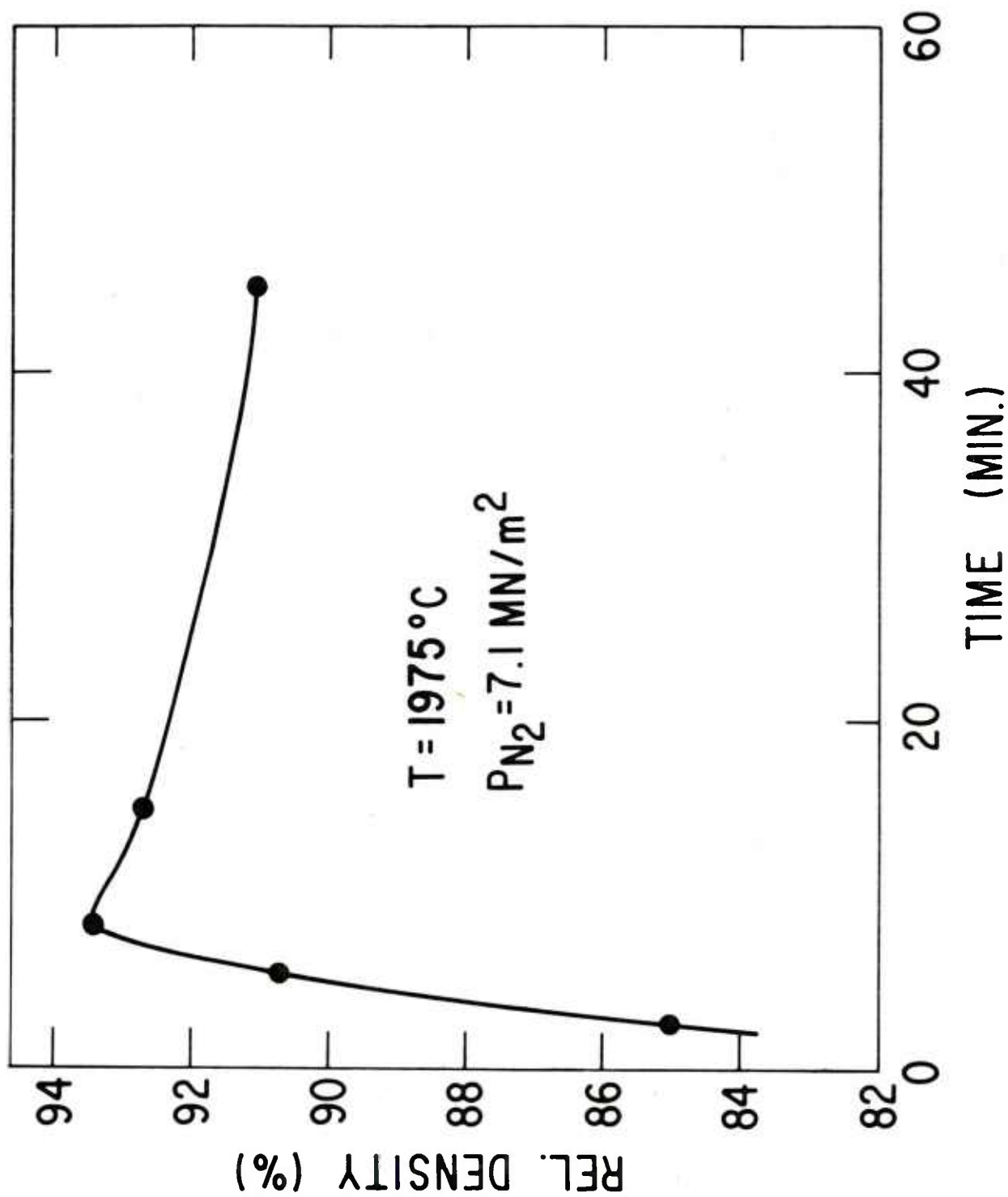
Figure 10. Relative density as a function of time for compacts of SN502-23A processed powder sintered at 1975°C in p_{N_2} = 7.1 MN/m² (70 atm.).

28

It was speculated that the maximum relative density of ~93% that occurs near the closed pore stage might be associated with the presence of unwanted volatiles evolving from inside the compact and/or poor chemical homogeneity of the starting processed SN502-23A powder. Therefore, a green compact of this powder was first calcined in 1 atm of N_2 at 1400^oC for 1 h followed by a standard sintering schedule. Again, there was no noticeable effect on relative density. Several compacts were then made from a new powder batch, SN502-59 processed powder (see Table I), which had the same amount (7 wt%) of $BeSiN_2$ additive milled into the Si_3N_4 powder for good chemical homogeneity. The compacts were then oxidized to an oxygen content of 3.02 wt% and then sintered at 1950 to 2000^oC for 15 min in 2.1 MN/m^2 of nitrogen pressure. Results of these experiments using SN502-59 processed powder were identical to those for compacts produced from the SN502-23A powder. Thus the results of these experiments suggested that the residual porosity of ~7% found for this composition of sintered Si_3N_4 was not associated with volatile species of foreign matter in the starting raw materials or with the formation of large pores resulting from the size or distribution of the 7 wt% $BeSiN_2$ densification aid.

The microstructures of various compacts sintered at different temperatures for various times in a constant P_{N_2} of 70 atm are shown in Figs. 11 and 12. The kinetics of development of the pore phase at 1975^oC shown in Fig. 11 reveal a fine pore phase (black structure) in the 85% dense sample (Fig. 11A) which decreases in amount as the relative density increases to 93.4% (Fig. 11B). When the sintering time increases from 8 to 45 min, Fig. 11C shows the average pore size increases from about 1 to 2.3 μm with a corresponding drop in relative density to 91%. Similarly, Fig. 12 shows the growth of pores from

(a)
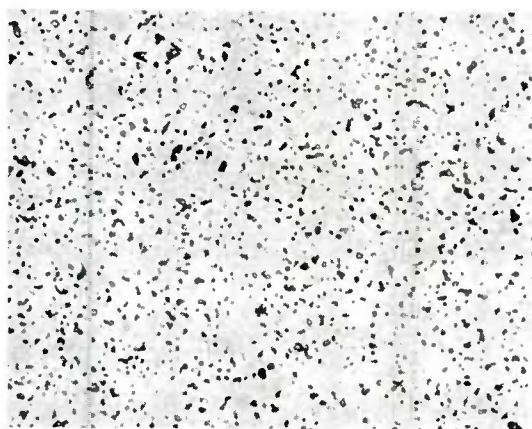
(b)
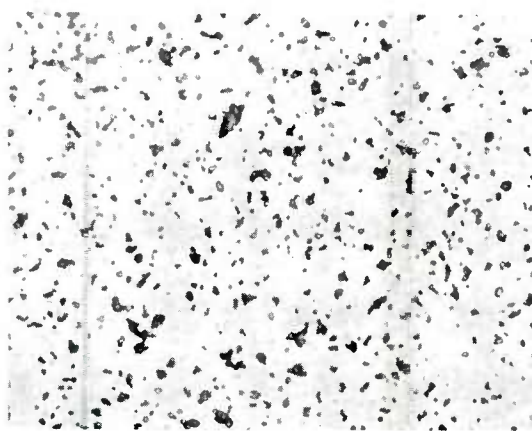
(c)

Figure 11. Kinetics of pore phase development
in sintered compacts of SN502-23A
processed powder at 1975°C in p_{N_2}
= 7.1 MN/m^2 (70 atm.) for times
of (A) 3 min., (B) 8 min. and (C) 45 min.
Mag. = 500X.

(a)
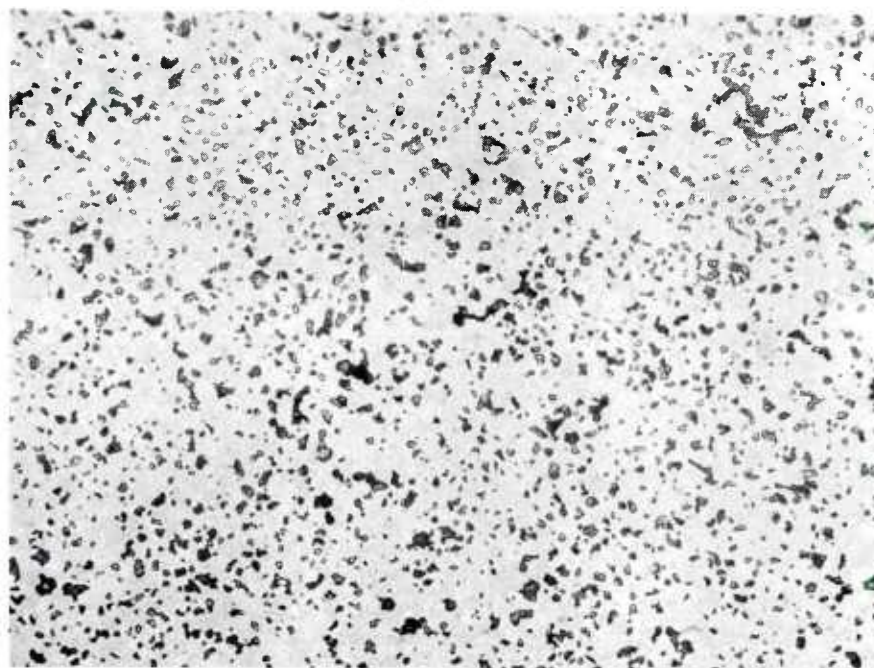
(b)

Figure 12. Typical microstructures of sintered compacts of SN502-23A processed powder after a 15 min. hold in p_{N_2} = 7.1 MN/m^2 (70 atm.) at (A) 1975°C and (B) 2050°C Mag. = 500X.

an average size of 1.5 μm (A) to 4.0 μm (B) by changing the sintering temperature from 1950 to 2050°C. Since the grains of the solid phase appear free of internal pores, apparently the residual pores are located at grain boundary intersections and grow most likely by a pore coalescence process. That is, the increase in average pore size may be associated with rapid grain growth and/or an Oswald ripening process, resulting in density regression of the sintered body. For this to happen the closed pores must be filled with N_2 gas which has a low solubility in the matrix and apparently decreases the driving force for densification to nearly zero. Thus, the density regression or volume expansion exhibited by a sintered specimen at T≥1975°C and at times greater than 8 min at 1975°C in 7.1 MN/m^2 (70 atm) of N_2 pressure appears to be caused by coalescence of N_2 gas-filled pores which have an internal gas pressure which exceeds the sum of surface tension plus applied pressure. A theoretical discussion of this problem is presented in a later section.

An understanding of the sintering mechanism was provided by energy dispersive X-ray analysis (EDXA) and X-ray diffraction of specimens sintered at 1800°C and 2000°C for 15 min in 7.1 MN/m^2 of N_2 pressure. These two specimens were selected because they represent, respectively, the very early stage (60% rel. density) and a later stage (rel. density = 91%) of densification. The EDXA results on both sintered specimens were essentially identical in that there were no detectable impurities acquired by the specimens during sintering in the BN crucible. The trace elements detected by this method were Mo and Cl which are impurities present in the starting SN502-Si_3N_4 powder. This information indicated that the densification process is probably not affected by the impurities present, excluding the possibility of B contamination from the BN crucible. Debye-Scherrer X-ray photographs of

the same two sintered samples showed the presence of strong β-Si_3N_4 lines and very weak lines of other crystalline phasaes. The lattice parameters of the β-Si_3N_4 phase formed in the specimen sintered to only 60% relative density at 1800°C were a = 7.587 $\pm$ 0.001 $\overset{o}{A}$ and c = 2.9012 $\pm$ 0.0004 $\overset{o}{A}$. Nearly identical lattice parameters were measured for the β-Si_3N_4 phase in the specimen sintered to 91% density of 2000°C. Since the lattice parameters of pure β-Si_3N_4 was measured as a = 7.596 $\pm$ 0.001 $\overset{o}{A}$ and c = 2.903 $\pm$ 0.001 $\overset{o}{A}$, it is apparent that nearly all densification takes place after the α-Si_3N_4 particles transform to a β-Si_3N_4 solid solution containing a significant amount of Be and O. Such β-Si_3N_4 solid solutions have been previously reported in the literature.[28] Many of the extra weak diffraction lines observed for both sintered samples could be accounted for if the trace phases were Si_2N_2O, Be_2SiO_4 and Si. Submicron "bright" particles, probably Si, can be observed in the microstructures shown in Figs. 11 and 12 by optical microscopy at higher magnifications. Since the phases Si_2N_2O and Be_2SiO_4 are oxygen-rich phases and the fact that Be_2SiO_4 is unstable and dissociates into BeO and liquid at T>1700°C,[29] it appears that these compounds perhaps crystallize during cooling from a liquid (glass) phase composed of Si, Be, O and N. This would imply that a liquid phase densification process occurs during sintering and that grain growth of the β-phase itself proceeds in the presence of a liquid phase.

Although many of the weak diffraction lines observed for the sintered samples were identified, a number of them were unaccounted for. The d-spacings for these weak-to-very-weak lines are roughly 11.9, 10.0, 6.0, 5.9 5.5, 5.05, 4.9, 4.0, 3.5, 3.2, 2.7, 2.05 and 1.94. The identification of these extra reflections are still a mystery and are not associated with $BeSiN_2$, BeO, or Be_3N_2.

33

B. **High Density (>99% Si_3N_4 Produced by the Gas Pressure Sintering (GPS) Method**

1. **Sintering Results**

A sintering method was discovered which increased the driving force for densification during sintering in order to overcome the undesirably low limiting densities of 92-93%. The idea was simply the application of a two-step, nitrogen pressurizing technique to the sintering body. First, the powder compact is sintered to the closed-pore stage which is typically achieved by firing for 15 min at 2000°C under 20 atm of N_2 pressure. After completion of this step and while the sample remains in the furnace, the second step consists of increasing the N_2 pressure to a higher P_{N_2} value, typically 70 atm for rapid densification. A pressure-temperature time cycle frequently used during the gas pressure sintering (GPS) process is illustrated in Fig. 7. A summary of some of the sintering results obtained on compacts of two high purity processed powders, SB502-23A and SN502-59, and the standard grade of processed powder of Stk 118 are presented in Table III. The SN502 Si_3N_4 powders contain 7 wt% $BeSiN_2$, and Stk 118 Si_3N_4 powder contains 3.5 wt% $BeSiN_2$.

The sintering results of runs 1 and 2 in Table III show that compacts of SN502-23A processed powder can be reproducibly densified to 97-98% of theoretical density with 1% weight loss by the designated GPS sintering treatment. Under the same conditions a compact of SN502-59 processed powder containing 3.02 wt% O (Run 3) did not respond to the GPS process using the two-step, N_2 pressurizing technique. However, a compact of this powder oxidized at 1000°C to an oxygen content of 3.7 wt% densified to 99.6% and exhibited a weight loss of 1% (Run 4). Run 5 shows that by lowering the temperature from 2000°C to 1940°C during the first step at 20

atm of N_2 pressure, the closed pore stage apparently did not develop and, consequently, a low relative density of 91.6% resulted. Run 6 reproduces Run 4 and further confirms the speculative reason for the lower density experienced by the compact of Run 5. Runs 7 and 8 illustrate that the second step of the GPS process can occur at temperatures 100 to 200°C below the initial sintering temperature and still give rise to sintered compacts of Si_3N_4 with relative densities greater than 98%. By using lower temperatures at which the higher N_2 pressure (70 atm) is introduced, the sintered specimens displayed lower weight losses (i.e., 1.3 vs 1.8%) and slightly higher porosities (1.4 vs 0.5%) and should consist of a finer average grain size.

The sintering results of Runs 9 and 10 in Table III were made on compacts of processed Stk 118 Si_3N_4 powder and found to be reproducible. Again, the oxygen content of the Si_3N_4 (probably by increasing the amount of glassy phase for higher oxygen contents) affects the sintering rate and how fast the closed pore stage develops. For example, for a compact having 1.47 wt% O (See Table I), the final density was ~92% after the compact experienced the GPS process at 2000°C. However, Run 10 shows that by increasing the oxygen content to ~2.6 wt% the compact sintered to nearly 97% relative density under the identical sintering treatment.

The kinetics of densification during the second step of the GPS process at 1920°C are shown in Fig. 13 for powder compacts of processed SN502-59 powder oxidized to an oxygen content of ~3.6 wt% and sintered in the first step at 2000°C for 15 min in a P_{N_2} of 20 atm. First of all, it was surprising to find a moderate increase in relative density from ~93 to 97.5% after 20 min in a P_{N_2} of 20 atm. An increase in density beyond ~93% at 2000°C was not observed in a P_{N_2} of 20 atm. Secondly, it was surprising that the densification rate was so sensitive to excess applied N_2 pressure above 20

TABLE III. SINTERING RESULTS ON Si$_3$N$_4$ COMPACTS EXPOSED TO A TWO-STEP, GPS PROCESS

| Run No.	Powder Type	Presintering Treatment	Sintering Treatment	Rel. Density	Linear Shrinkage (%)	Weight Loss (%)
1	SN502-23A Processed	--	15 min-2000°C-20 atm N$_2$ + 18 min-2085°C-70 atm N$_2$	97.5	20	1.4
2	"	--	"	97.9	20	1.2
3	SN502-59 Processed Powder Oxidized at 1000°C to 0-content=3.02 wt%		"	91.9	19.7	0.3
4	"	Compact oxidized to 0-content ~3.7 wt%	"	99.6	22.5	1.0
5	"	"	15 min-1940°C-20 atm N$_2$ + 10 min-2000°C-70 atm N$_2$	91.6	19.5	1.9
6	"	"	15 min-2000°C-20 atm N$_2$ + 12 min-2000°C-70 atm N$_2$	99.4	22.8	1.8
7	"	Compact oxidized to 0-content ~3.5 wt%	15 min-2000°C-21 atm N$_2$ + 20 min-1900°C-70 atm N$_2$	99.7	22.8	1.6
8	"	"	15 min-2000°C-21 atm N$_2$ + 30 min-1800°C-70 atm N$_2$	98.6	22.4	1.3
9	Stk 118 Processed	--	15 min-1990°C-23 atm N$_2$ + 12 min-2000°C-70 atm N$_2$	92	15	+0.7
10	"	Compact oxidized at 1000°C to 0-content ~2.6 wt%	"	96.8	17.6	2.7
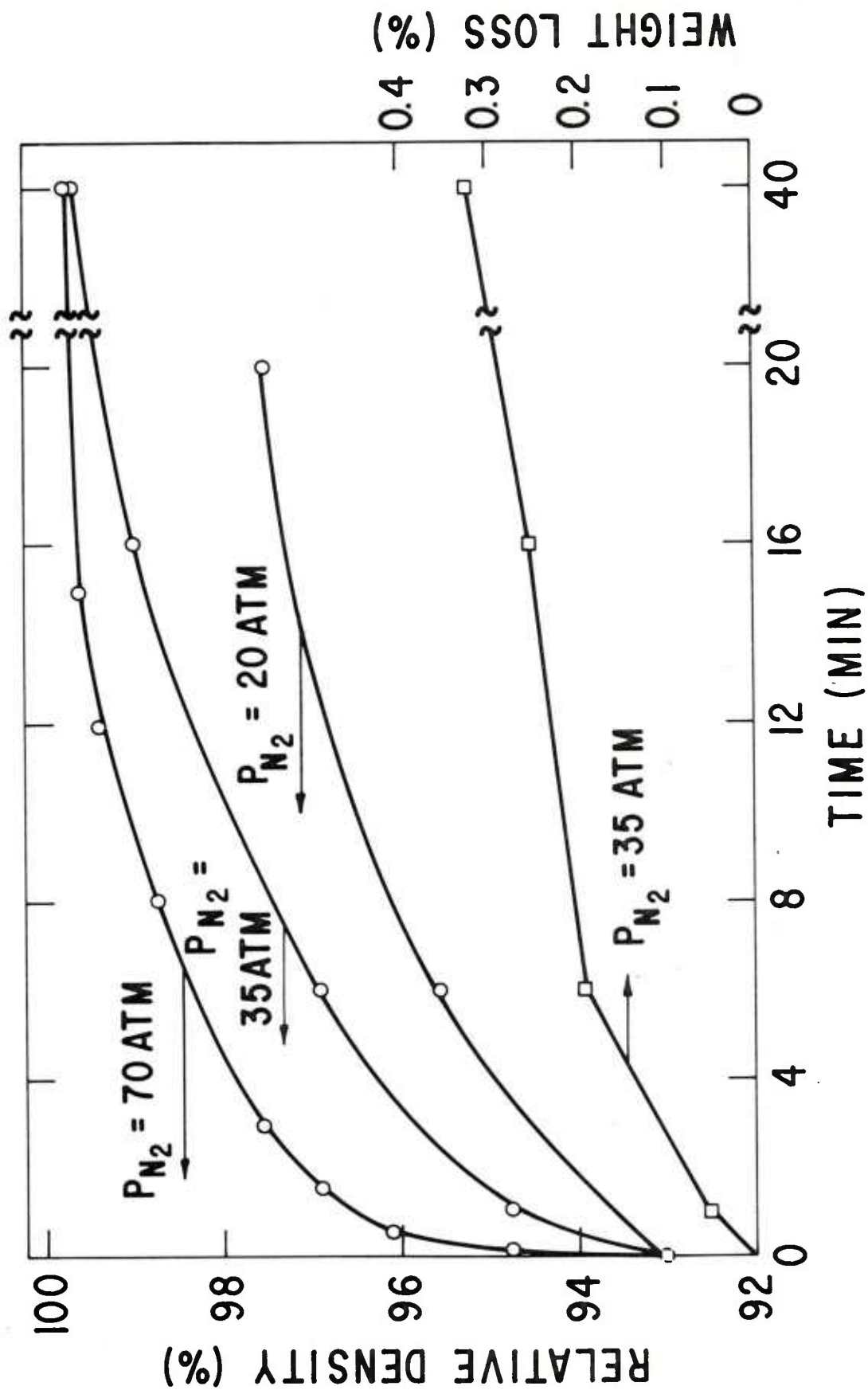
Figure 13. Kinetics of densification and weight loss for compacts of SN502-59 processed powder in various nitrogen pressures during the second step of the GPS process at 1920°C.

37

atm. For example, Fig. 13 shows that by nearly doubling the P_{N_2} to a value of 35 atm the driving force for densification apparently increases markedly because nearly full density (99.7%) is reached in about 40 min at 1920°C. Again, doubling the P_{N_2} to 70 atm results in rapid densification with nearly full density attained in only ∿15 min. The densification process proceeds with a small amount of weight loss designated in Fig. 13 for samples sintered in a P_{N_2} of 35 atm. Some speculaton on reasons why low pressures of N_2 (<100 atm) gas aids densification of sintered Si_3N_4 is discussed in a later section.

Once Si_3N_4 is gas pressure sintered to a high relative density of 99.7% in, for example, 70 atm of N_2, the resulting material is very resistant to density regression in lower N_2 pressures. For instance, there was no significant drop in density after being exposed for 30 min in 20 atm of N_2 at 2000°C. Furthermore, no change in density was found for GPS Si_3N_4 exposed to 1 atm of P_{N_2} at 1650°C for 1 h. In the latter case it was satisfying to also find out that only a very small weight loss of ∿0.04% accompanied this heat treatment. On the other hand, the relative density dropped to ∿96% and the weight loss increased to ∿0.5% by exposing GPS Si_3N_4 to 1800°C for 1 h in 1 atm of N_2. The overall results point to a very stable form of Si_3N_4 for use at temperatures up to about 1700°C in nitrogen.

2. Characterization of Microstructure

The microstructure of GPS Si_3N_4 was characterized by using optical, scanning and transmission electron microscopy. Fig. 14 shows the typical microstructure of a polished section of sintered Si_3N_4 having a relative density of 99.6% (Run 4 in Table III). The sintered compact is indeed very dense, with only a few rounded pores (black phase), as shown in photomicrographs 14A and B taken at the low magnifications. A few small bright spots of probably Si begin to be resolved at a magnification of 500X. Reflected

(a)
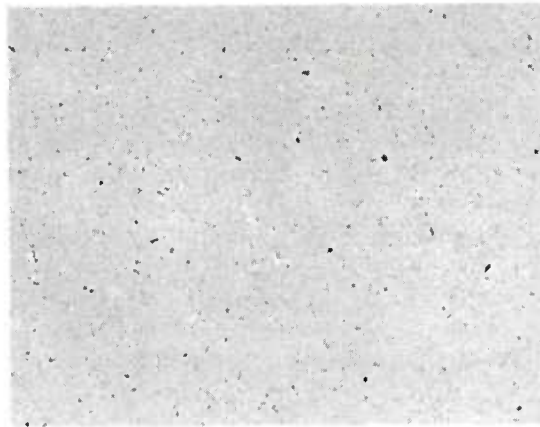
(b)
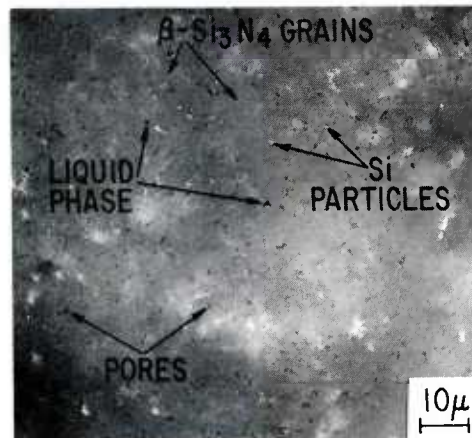
(c)

Figure 14. Typical microstructure of 99.6% dense, GPS Si_3N_4 derived from SN502-59 processed Si_3N_4 powder.
(A) Mag. = 250X,
(B) Mag. = 500 X and
(C) scale as specified on photograph.

light microscopy using an oil immersion objective lens at high magnification (Fig. 14C) provides invaluable microstructural information. The microstructure is characterized by (1) a few, small (0.5μm) intergranular pores (black phase), (2) submicron Si particles apparently associated with liquid phase pockets (dark grey phase) located at intersections of growing β-Si_3N_4 grains (grey phase) and (3) interference fringes and subsurface light scattering (light grey areas) indicative of highly dense, translucent regions. A good photograph of several large pockets of liquid phase (dark grey) is illustrated in Fig. 15. This micrograph also shows that some of the β-Si_3N_4 grains are faceted and quite hexagonal in shape. Faceting is pronounced in β-grains bordering larger pockets of liquid phase. X-ray diffraction patterns using the diffractometer with monochromated CuK_α-radiation showed only the presence of a β-Si_3N_4 solid solution. X-ray diffraction using the Debye-Scherrer method showed that besides the major phase of β-Si_3N_4 solid solution (a = 7.589 $\pm$ 0.001 $\overset{o}{A}$ and c = 2.9039 $\pm$ 0.0004 $\overset{o}{A}$) trace amounts of Si_2N_2O and Be_2SiO_4 were present in addition to the same extraneous lines as observed previously for lower density samples (92%) were also present in this highly-dense sample.

The delineation of the β-Si_3N_4 grains is difficult to reveal by standard ceramographic techniques. Only a partial outline of some of the largest grains can be observed in Figs. 14C and 15. Typically, caustic etching with a mixture of LiOH, NaOH and KOH has been found to be partly successful, but it produced considerable amounts of porosity due to preferential attack of the liquid and pore phases. This phenomenon is illustrated in Fig. 16 where the "black" triangularly regions at intergranular positions were previously-filled with liquid phase. The grain structure is partially discernible and composed of a mixture of elongated grains up to 15 microns in length and equiaxed grains having dimensions between 1 and 4 microns. The best resolu-

tion of the size and morphology of the β-Si_3N_4 grains was achieved by using thin sections viewed in transmitted polarized light. A typical photomicrograph illustrated in Fig. 17 shows elongated β-Si_3N_4 grains as long as 25 μm and with an average diameter of 3 μm. This type of microstructure showing an intergrowth of elongated (lath-shaped) β-Si_3N_4 grains is typical of Si_3N_4 with high mechanical strength.[24]

High resolution TEM provided additional information about the nature of the intergranular phases present in sintered Si_3N_4 (97.9% density) prepared in Run No. 2 (Table III). Only occasional Si particles (black in contrast) can be observed at 3- and 4-grain intersections at magnifications up to $\sim$100,000 X (see Fig. 18A). A typical micrograph such as this also shows thickness fringes outlining some grain boundaries with proper orientation to the electron beam. In some cases a liquid phase pocket (see Fig. 18B) is observed at 3- and 4-grain intersections of the β-Si_3N_4 grains. The dihedral angle between the solid and liquid phases appears to be relatively low but not zero. In Fig. 19 the use of higher resolution lattice fringe techniques on two neighboring β-Si_3N_4 grains near a liquid phase pocket (light grey phase) shows a thin (10 $\overset{\circ}{A}$) film of "liquid" extending down the grain boundary. The $(10\bar{1}0)$ lattice fringes (d-spacing $\approx$6.6 $\overset{\circ}{A}$) are present in the upper β-Si_3N_4 grain whereas the $(11\bar{2}0)$ lattice fringes (d-spacing $\approx$3.6 $\overset{\circ}{A}$) are just visible in the lower β-Si_3N_4 grain. Several boundaries of this type did contain a thin film which is apparently a liquid phase. Nevertheless, it is difficult to generalize whether all grain boundaries have a thin film because an insufficient number of neighboring β-Si_3N_4 grains could be found with simultaneous low-index diffraction zones within the tilting range of the microscope. Clearly, these TEM results suggest that for the Si_3N_4 compositions investigated here, densification takes place via a liquid-phase sintering mechanism.
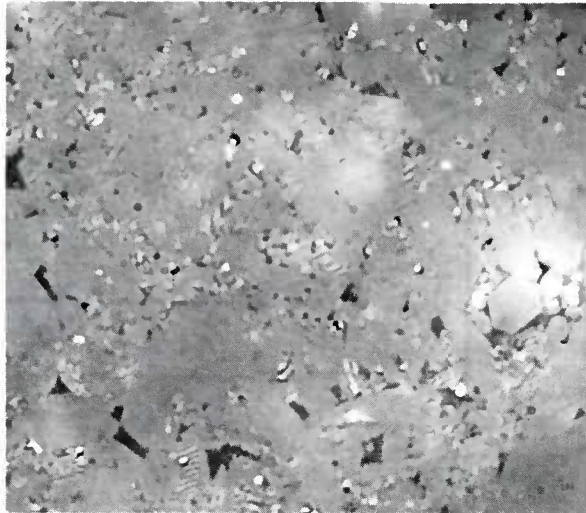
Figure 15. Microstructure of 99.5% dense, GPS Si_3N_4 showing liquid-phase pockets and several hexagonal grains of β-Si_3N_4. Mag. = 2000X.
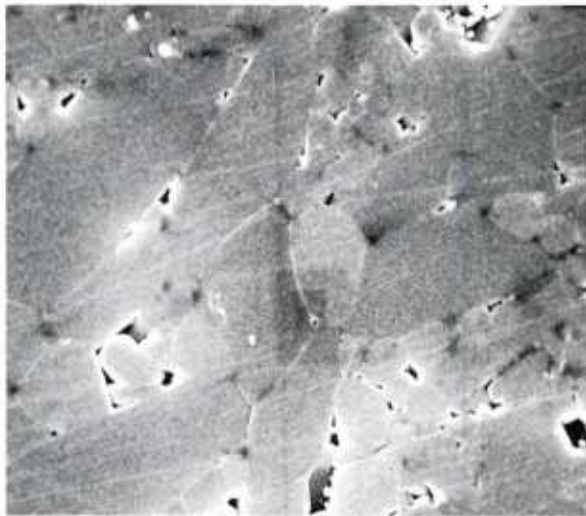

Figure 16. A polished and caustic-etched microstructure of GPS Si_3N_4 showing the beta Si_3N_4 grains. SEM photomicrograph at a Mag. = 3,500X.
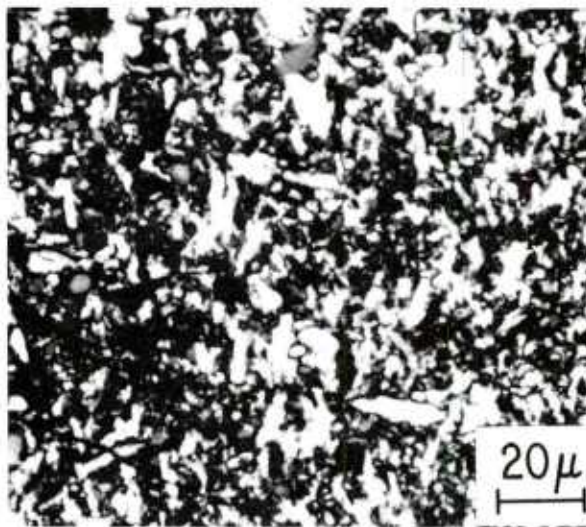
Figure 17. Grain structure revealed in GPS Si_3N_4 by viewing through a thin section (<50 microns) using transmitted polarized light.
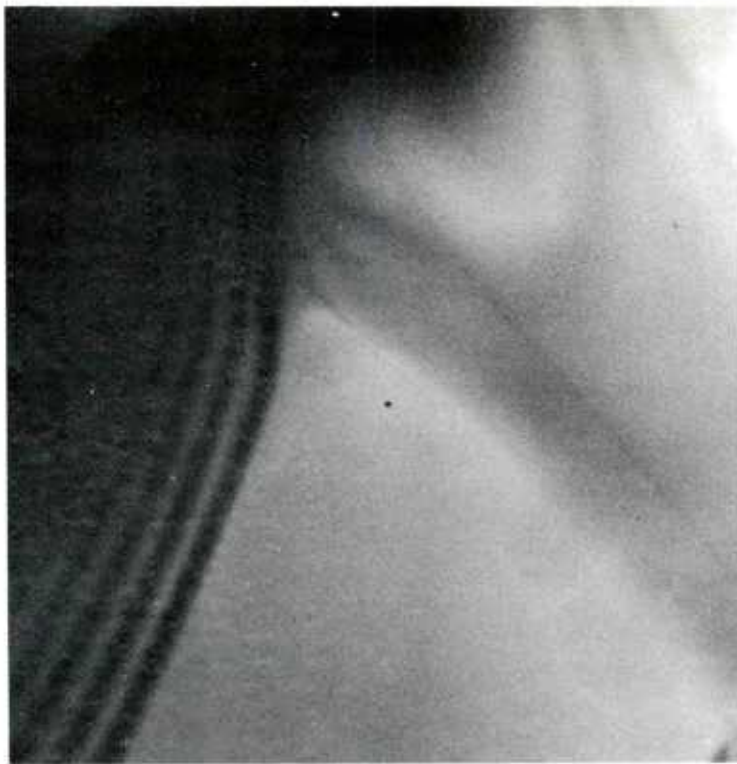
(a)
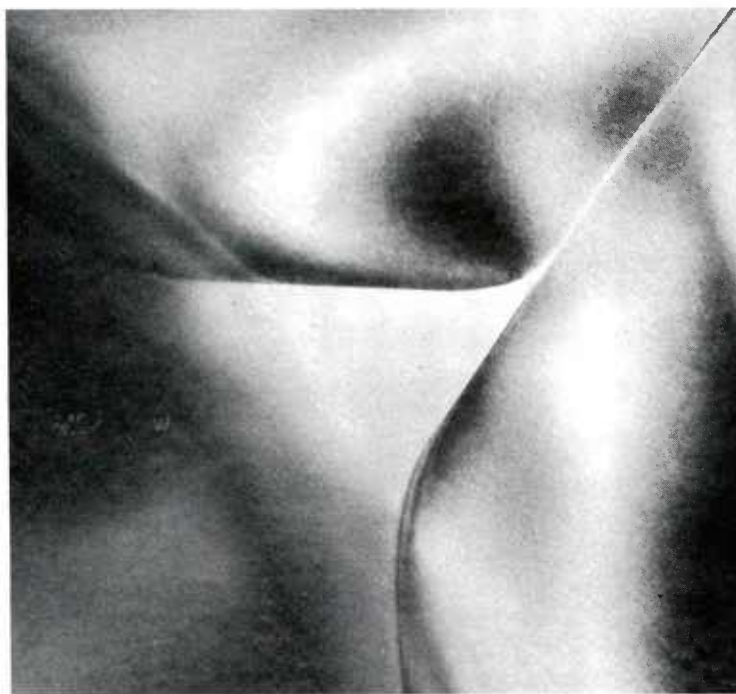
(b)

Figure 18. TEM photomicrographs of grain boundary regions in GPS Si_3N_4. (A) Typical region with occasional Si particle (70,000X) and (B) typical liquid (glassy) phase pocket (200.000X).

43

Figure 19. Grain boundary film between two β-Si$_3$N$_4$ grains which are both strongly diffracting to permit lattice fringe images. Mag. = 1.17 x 10^{6}X.

VII. SOME THEORETICAL CONSIDERATIONS ABOUT FINAL STAGE SINTERING OF Si_3N_4 IN NITROGEN GAS PRESSURE

The gas pressure sintering (GPS) process described herein is used primarily for its effectiveness during the final stages of the sintering process, i.e., when the pore phase transforms into discrete, disconnecting pores that are filled with gas pressure at the seal-off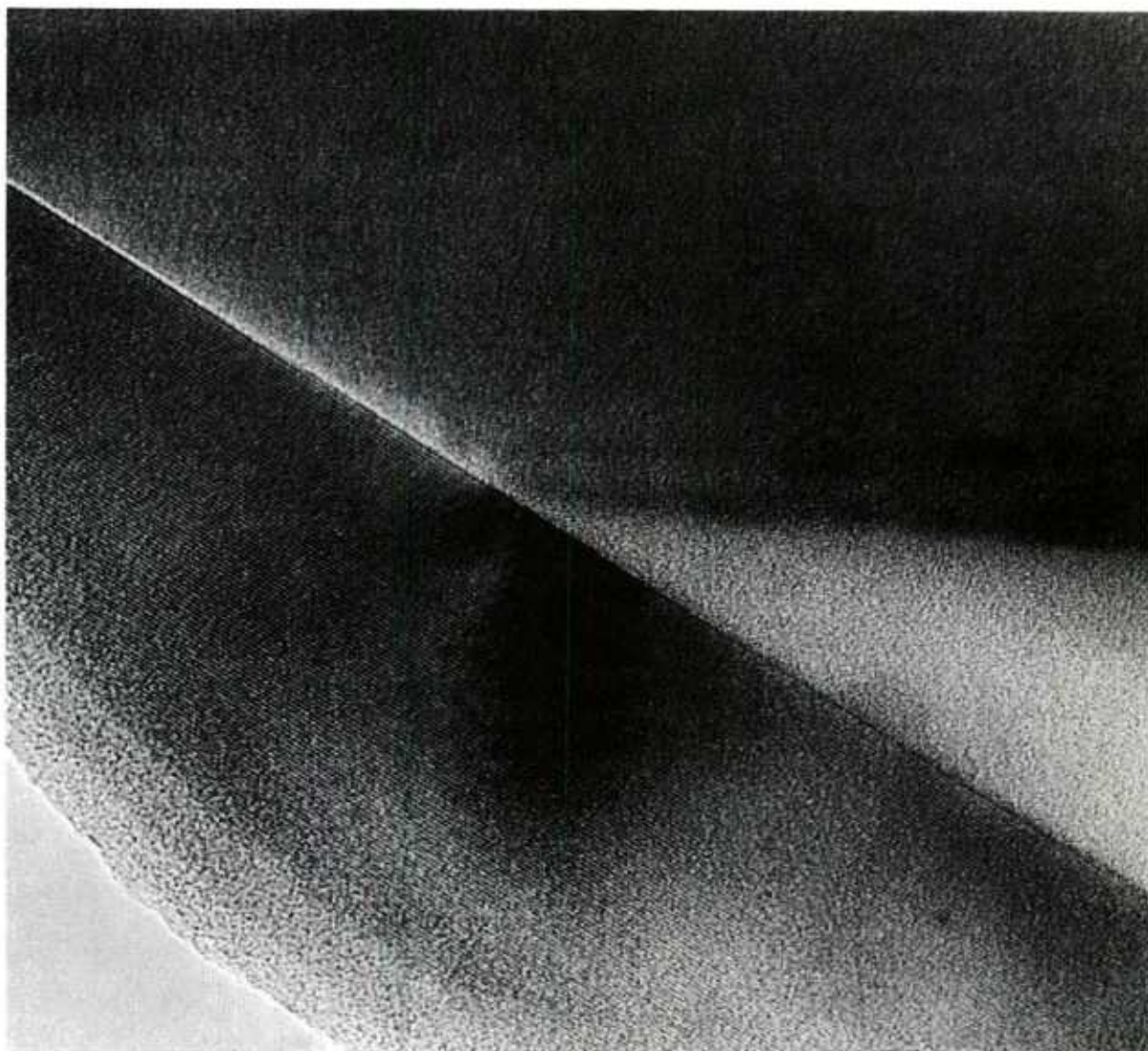 conditions. In order to help explain some of the sintering data presented in Figs. 9, 10 and 12 and Table III, theoretical equations are developed which give guidance for the expected changes in the average equilibrium pore size filled with an insoluble gas of a given pressure and the corresponding maximum relative density expected at equilibrium.

A. The Equilibrium of Single, Gas-Filled, Spherical Pores

The pressure inside of a closed pore at equilibrium is

$$P_e = \frac{2\gamma}{r_e} + P_a \tag{12}$$

where γ is the solid-vapor surface energy, r_e the equilibrium pore radius and P_a the external gas pressure over the sintering body.

P_e can also be defined from the ideal gas law.

$$P_e = nRT/V_e \tag{13}$$

where

$$n = P_oV_o/RT_o \tag{13a}$$

$$V_e = (4/3)\,\Pi\, r_e^3 \tag{13b}$$

$$V_o = (4/3)\,\Pi\, r_o^3 \tag{13c}$$

Here, n is the number of moles of gas inside a spherical pore at radius r_o at the initial conditions of pore closure, i.e., at a pressure P_o and temperature T_o.

The parameters T and V_e are the temperature and individual pore volume after equilibrium is established. Substitution of Eqs. (13a), (13b) and (13c) into Eq. (13) gives

$$P_e = \frac{P_o r_o^3 T}{r_e^3 T_o} \qquad (14)$$

By equating Eqs. (12) and (14) and rearranging, the following general equation is obtained

$$P_a r_e^3 + 2 \gamma r_e^2 = \frac{P_o T}{T_o} r_o^3 \qquad (15)$$

Equation (15) gives the equilibrium radius of a pore, r_e, filled with insoluble gas which had an initial radius of r_o at a temperature T_o and pressure P_o. Since it is experimentally observed that closure takes place at a porosity (ϕ_o) of $\sim 8\%$ in the sintering body, then if the spherical pores of initial radius r_o do not coalescence with one another, the final relative density, D_e, of the body after equilibration of the gas-filled pores is

$$D_e = 1 - \phi_e . \qquad (16)$$

It can be shown that for the case of individual gas-filled pores;

$$D_e = 1 - \phi_o \left(\frac{r_e}{r_o}\right)^3 . \qquad (17)$$

The calculation of the equilibrium pore radius, r_e, and relative density, D_e, at a temperature of $2000^\circ C$ in various gas pressures was determined by using Eqs. (15) and (17) and taking $\gamma = 10^3$ ergs/cm^2. Table IV lists these

values for two initial pore radii typically found in the microstructure of sintered Si_3N_4 (see Figs. 11) at pore closure where the relative density is ⋏92%. For pore radii of 0.5 and 1.0 microns that contain between 15 and 70 atm of N_2 gas at pore closure, the relative density should increase from ⋏94 to ⋏99% upon equilibration of the sintering body. Clearly, these results are in direct conflict with the sintering data in Figs. 9 and 10, which show that relative densities greater than ⋏93% are not only attained but, density regression occurs. Table V shows that if a sintered compact is first equilibrated in 20 atm of gas pressure and then re-equilibrated in higher gas pressures of 35 and 70 atm at 2000°C, the equilibrium (final) relative density should increase from 96.5-98.1% (see Table IV) to 97.5-98.9%. This same result is obtained even if the temperature of equilibrium is reduced from 2000 to 1900°C. The small increase in relative density of 1-2% by first equilibrating in 20 atm followed by re-equilibration in higher gas pressures of 35 and 70 atm can not alone explain the marked enhancement of densification observed for the gas pressure sintering of Si_3N_4 shown in Table III and Fig. 13.

B.   The Effect of Pore Coalescence on Final Density

So far, we have theoretically discussed what happens to individual, gas-filled pores of spherical geometry that continue to decrease in radii during equilibration after pore closure. However, it was experimentally verified that the average pore size increases with time at temperature and is a consequence of pore coalescence probably via rapid grain growth. The major effect of pore coalescence is to cause lower final relative densities than those predicted using Eqs. (15) and (17). Neglecting the details of the derivation, it can be shown that the final general equation that considers the effect of pore coalescence on the equilibrated pore radius is expressed by

TABLE IV CALCULATION OF THE EQUILIBRIUM PORE RADIUS AND RELATIVE DENSITY FOR ϕ_c=8%, T=T_o=2000°C, AND THE SAMPLE ALLOWED TO EQUILIBRATE AT CONSTANT PRESSURE (P_a=P_o).

Pressure (Atm)	r_o (microns)	r_e (microns)	D_e (%)
15	0.5	0.28	98.6
15	1.0	0.70	97.2
20	0.5	0.31	98.1
20	1.0	0.76	96.5
35	0.5	0.37	96.8
35	1.0	0.84	95.2
70	0.5	0.42	95.2
70	1.0	0.91	93.9

TABLE V CALCULATION OF THE EQUILIBRIUM PORE RADIUS AND RELATIVE DENSITY FOR ϕ_o =8%, T=T_o=2000°C, AND THE SAMPLE ALLOWED TO EQUILIBRATE AT P_a=P_o=20 ATM. FOLLOWED BY RE-EQUILIBRATION AT 35 AND 70 ATM OF N_2 GAS PRESSURE.

Pressure (Atm)	r_o (microns)	r_e (microns)	D_e (%)
35	0.50	0.29	98.5
35	1.0	0.69	97.5
70	0.50	0.26	98.9
70	1.0	0.58	98.5

$$\left(\frac{2\gamma}{r_{e_2}} + P_{a_2}\right) r_{e_2}^3 = \frac{n_2 T_2}{n_1 T_1} \left(\frac{2\gamma}{r_{e_1}} + P_{a_1}\right) r_{e_1}^3 , \tag{18}$$

where pores of equilibrium radius r_{e_1}, containing n_1 moles of gas at an applied

gas pressure of P_{a_1} and temperature T_1, coalesce and re-equilibrate at a

second set of conditions of P_{a_2}, n_2 and T_2 to establish a new radius r_{e_2}. For

a single coalescence process in which two equal-sized pores of equilibrium

radius r_{e_1} coalesce into a single pore of radius r_{e_2}, n_2 is just equal to twice

n_1. For a second coalescence process, $n_2 = 4 n_1$, and so on. The

determination of r_{e_1} is first calculated from Eq. (15) by choosing a given value

of r_o and taking $\gamma = 1000$ ergs/cm^2. Then r_{e_2} is calculated from Eq. (18) for

the sintering conditions desired.

A summary of the results on coalescence of gas-filled pores of initial

radius $r_o = 0.5$ microns is given in Table VI for three consecutive coalescence

processes under different sintering conditions. Three pore coalescences is

equivalent to doubling the average grain size, assuming cubic grains with a

pore at every cube corner. The first two examples in Table VI are

calculations of the equilibrium pore radius, r_{e_2}, and relative density, D_{e_2},

after 1 to 3 coalescence processes in a constant applied pressure of 70 and 20

atm and a constant temperature of 2000°C. The equilibrium pore radius

increases from 0.55 to 0.91 microns and the relative density drops from 94.7

to 93.9% in the first example. These pore radii are very similar to those

observed in sintered microstructures in Fig. 11 under nearly the same

experimental conditions. The trend of decreasing density with increasing

number of coalescence processes (or increasing sintering time) predicted

agrees with experimental observations (see Fig. 10) except that the absolute

values of relative density predicted are higher than those observed. Similar

conclusions are reached by comparing the predicted D_{e_2} values calculated in

the second example of Table VI with experimental data on the density

TABLE VI   THE EFFECT OF COALESCENCE OF GAS-FILLED PORES OF INITIAL RADIUS OF 0.5μ AT PORE CLOSURE ON THE EQUILIBRIUM PORE RADIUS, r_{e_2}, AND RELATIVE DENSITY, D_{e_2}.

Coalescence	Example 1 $P_{a_2}=P_{a_1}=70$ Atm, $T_2=T_1=2000°C$		Example 2 $P_{a_2}=P_{a_1}=20$ Atm, $T_2=T_1=2000°C$		Example 3 $P_{a_2}=70$ Atm, $P_{a_1}=20$ Atm $T_2=1900°C$, $T_1=2000°C$	
	r_{e_2} (microns)	D_{e_2} (%)	r_{e_2} (microns)	D_{e_2} (%)	r_{e_2} (microns)	D_{e_2} (%)
1	0.55	94.7	0.42	97.6	0.33	98.8
2	0.71	94.3	0.57	97.1	0.44	98.7
3	0.91	93.9	0.76	96.5	0.57	98.5

50

decrease with time during sintering at 2000°C in20 atm of N_2 gas. The last example in Table VI simulates the typically-used GPS process for Si_3N_4. In this case the coalescence of gas-filled pores cause rather little density regression when the applied pressure is increased from 20 to 70 atm and the temperature reduced from 2000° to 1900°C.

The major disadvantage of using the theory of coalescence of gas-filled pores to explain the experimental density results from sintering experiments carried out near and above 2000°C is that there is poor agreement in the absolute magnitude of the final density, even when allowing for the possibility of non-equilibrium conditions during actual sintering experiments and the consideration of pore size distribution in the theory. Specifically, the predicted density drop caused by pore coalescence can not explain the very low relative densities of 88-89% experimentally observed to occur in sintered samples containing closed porosity. The reason is simply that the final relative density predicted from coalescence of gas-filled pores can not drop below 92% relative density, i.e., the density attained at pore closure. This is because at the instant of pore closure each gas-filled pore has not had a chance to contract due to surface tension forces ($2\gamma/r$) and, hence, the entire body exhibits its maximum volume of porosity. The cause of the low relative densities of 88-89% observed for sintered Si_3N_4 near and above 2000°C in 20 to 70 atm of N_2 pressure is most likely associated with the generation of gas inside closed pores in the sintered body. The "bloating" effect is probably related to the thermal decomposition of the SiO_2-rich glassy phase into gaseous species such as SiO and N_2. This increase in the number of moles of gas inside the closed pores increases the gas pressure inside a pore and can result in equilibrium relative densities significantly lower than 92%.

The high relative densities of 99.7% attained by the gas-pressure-sintering process illustrated in Fig. 13 for an applied gas pressure of 70 atm can be at least partly understood from Example 3 in Table VI. In this case the maximum relative density of 98.5 to 99% can be expected for sintered samples having pores coalesce 1 to 3 times for an initial pore radius of 0.5 microns at pore closure in 20 atm of N_2 pressure at 2000°C followed by re-equilibration of these pores in 70 atm of N_2 pressure at 1900°C. If the initial pore radius at pore closure was 0.25 microns, a value undoubtedly representing a lower limit, the maximum relative density attainable increases to 99.0 or 99.3% by assuming 1 or 3 pore coalescence processes. The significantly higher relative densities of 99.7% experimentally observed suggests that at least some of the N_2 gas inside of the pores is soluble in the surrounding matrix. Microstructural observations show that pores are located at inter-granular regions where also SiO_2-rich liquid and Si liquid phases reside. It is speculated that N_2 gas is absorbed by one or both of these phases by reducing N to N^{3-} and oxidizing Si (or possibly Si^{2+}) to Si^{4+}. Further support for nitrogen solubility in GPS Si_3N_4 can be deduced from annealing experiments on dense (99.7%) samples at 1900 and 2000°C. Here, by reducing the total gas pressure from 70 to 20 atm there was no significant drop in the relative density after 30 min of annealing time. The kinetics of pore "swelling" via dissolved nitrogen reforming as gaseous molecules inside existing pores may be just too slow to be detectable after short annealing times because of the large reduction in the number density of available pores caused by pore coalescence in the 99.7% dense sample preceeding the annealing treatment. Finally, it is noteworthy that the disappearing nitrogen gas inside the closed pores is most likely accommodated by solubility into the matrix phase(s) and not by gas diffusion out of the sintered body. If nitrogen

gas is lost by gas diffusion out of the sintered sample, then a gradient in porosity from the interior to the exterior surface should be observed in the sintered compact. Polished sections of compacts sintered to relative densities of $\approx$96.0 and 97.5% during the second step of the GPS process at 70 atm of N_2 pressure (see Fig. 13) showed no obvious difference in the amount of porosity present in the surface and interior regions.

VIII. PROPERTIES OF GPS Si_3N_4

A. Room Temperature and High Temperature Strength

Sintered billets having greater than 99% relative density (except for one case) were used for making mechanical test bars. The final dimensions of sintered billets for GPS Si_3N_4 weighing $\sim$15 g were 26 mm long x 15 mm diameter. All sintered billets used for preparing test bars had initial beryllium and oxygen contents of $\approx$0.9 and 3.6 wt%. In one case the Be and O contents of a sintered billet were measured to be $\approx$0.8 and 3.0%, respectively.

Test bars nominally 2.5 x 2.5 mm in cross section and 26 mm long were diamond sliced from the sintered billets and subsequently surface ground. Five test bars cut from billet #35 had their faces finished with a 45 micron diamond wheel and their long edges chamfered with 65 micron diamond paste. These bars were evaluated for room temperature strength in a 3-pt bending mode using a span length of 1.9 cm and an Instron crosshead speed of 0.5 mm/min. Considerable scatter was noted in these early strength measurements with values of strength ranging from 358 MNm^{-2}(52,000 psi) to 640 MNm^{-2}(93,000 psi). The average strength had a value of 490 MNm^{-2}(71,000 psi). Microscopic examination of the fractured surfaces showed the fractured origins in each instance to occur at a corner (chamfered edge), indicating

that some improvement in fracture strength could be expected if the surface finish of the faces and edges of bars were improved.

Three remaining bars from billet #35 and 5 test bars from billet #38 (same composition and sintering treatment as billet #35) were finished on the 4 faces with a 500 grit diamond wheel and the 4 long edges were chamfered with 15 micron diamond. The average fracture strength of the 3 bars from billet #3 was 553 MNm^{-2}(80,200 psi) which is close to the average strength of 563 MNm^{-2}(81,650 psi) found for the 5 bars prepared from billet #38. These 8 strength values are represented as a group in a Weibull plot of probability-to-failure vs the fracture strength (modulus of rupture) shown in Fig. 20. The average strength for the 8 bars combined was 560 ± 68 MNm^{-2} with a plotted Weibull modulus of 9.1. Microscopic examination again showed that the fracture origins were located on or near the tensile surface of each bar.

It was important to determine if the critical surface flaws limiting fracture strength were related to large ($\geq$10 microns) powder aggregates or inclusions (metallic particles introduced during ball milling) present in the final processed powder composition. In order to study this possibility, a 50 g batch of SN502-87 Si_3N_4 processed powder was strained through an 8 micron, nylon screen using water as a liquid medium and tetramethylammonium hydroxide as a dispersing agent. The solids content was ∿20 volume %, and the pH of the suspension was ∿10. Two sintered billets, #77 and #78, were made from the "screened" powder and had the same nominal composition and sintering schedule as used for billets #35 and #38. The relative density of sintered billets #77 and #78 was 99.2 and 99.3%, respectively, and the weight loss during sintering was ∿1 wt%. Ten test bars of the same size and surface finish as bars made from billet #38 were prepared and mechanically tested in the same manner. These strength results are also shown in Fig. 20. The
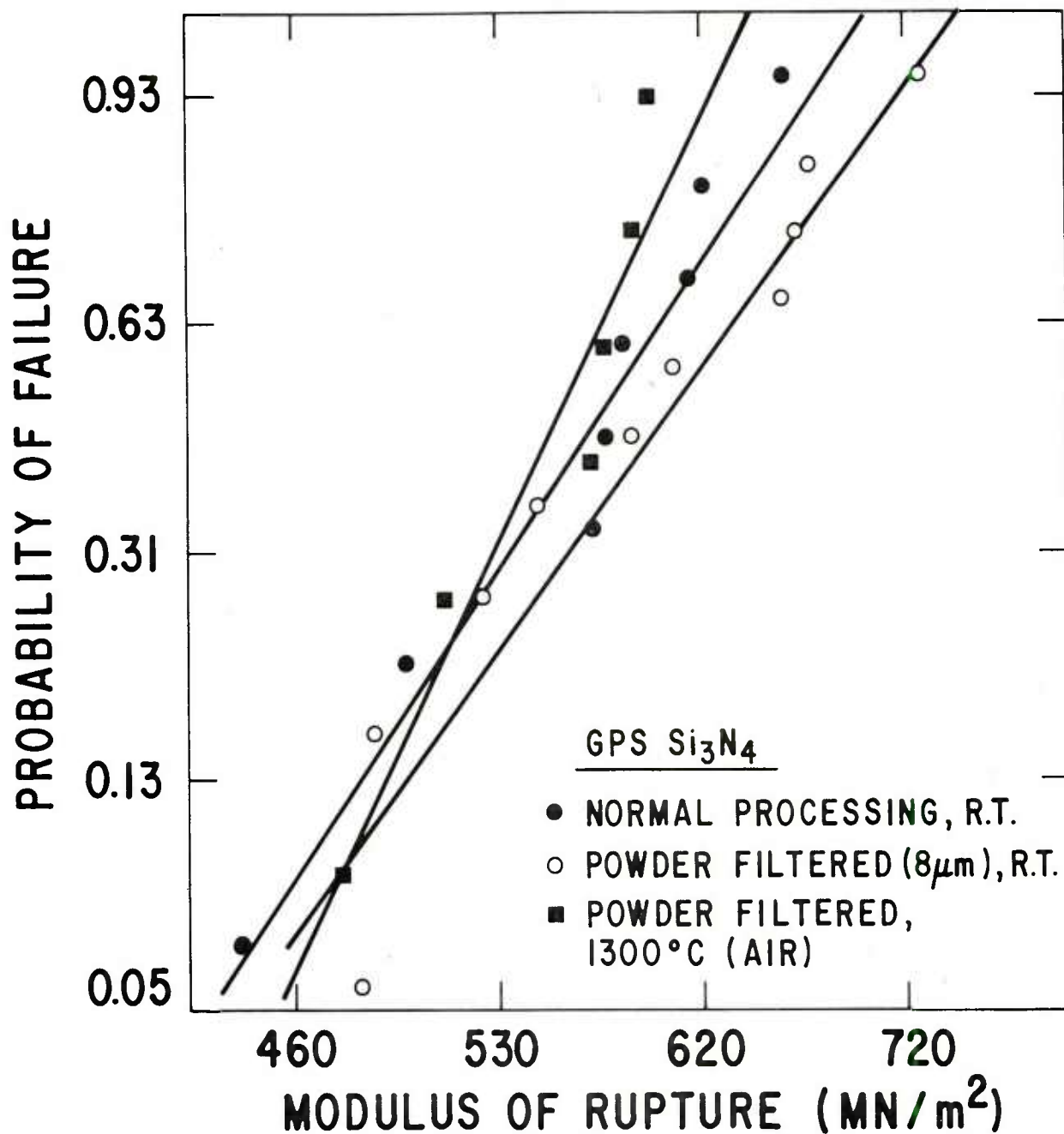
Figure 20. A Weibull plot of probability-of-failure versus modulus of rupture (3-pt. bend) for GPS Si_3N_4, prepared from normal and powder-filtered processing methods, and mechanically tested at room temperature and $1300^\circ C$.

average strength measured was 597 MNm^{-2}(86,540 psi) with a standard deviation of $\pm$ 83 MNm^{-2}(12,086 psi). The plotted Weibull modulus for the 10 data points was 8.3. By observation of the fracture surfaces of each broken bar, the critical flaw that limits strength originated on the tensile surface of each bar. Therefore, the critical flaws (cracks) originate from the finishing operation during specimen preparation. Based on the known fracture thoughness value (K_c = 2.9 MNm$^{-3/2}$) and the average strength for the GPS Si$_3$N$_4$ material, the average flaw size calculated was about 6 microns.

It is interesting to compare the average strength value of 597 MN/m^{-2} found for sintered Si$_3$N$_4$, derived from processed powder screened through an 8 micron screen, with the average strength value of 560 MN/m^{-2} found for sintered Si$_3$N$_4$ prepared by standard processing procedures (no screening of powder aggregates greater than 8 microns). Obviously, only a 7% increase in average strength is observed by using the screened powder. It is concluded that this treatment has little beneficial effect on reducing the size of surface flaws on the test bars during the finishing operation. Furthermore, the true bulk strength of GPS Si$_3$N$_4$ at room temperture is probably appreciably higher than the currently observed strength of $\approx$ 600 MNm^{-2}.

The high temperature strength of GPS Si$_3$N$_4$ was measured in air at 1300°C. The short-term fracture strength of 6 test bars (2.5 x 2.5 x 26 mm) made from billet #78 was measured in 3-pt berding using a span of 1.9 cm and crosshead speed of 0.13 mm/min. Each test bar was placed on SiC supports and held at 1300°C for 15 min before loading it to failure. From the fracture strengths measured and plotted in Fig. 20, the average strength at 1300°C for GPS Si$_3$N$_4$ is 553 MNm^{-2} (80,200 psi) $\pm$ 48 MNm^{-2}. The plotted Weibull modulus was determined to be 12.9. These results indicate that the short-term

56

strength retention at 1300°C in air is about 93% of the room temperature strength. Furthermore, the Weibull modulus appears to increase from 8.3 to 12.9 by exposing the test bars to an elevated temperature of 1300°C for 15 min in air. For more meaningful Weibull values, much more mechanical testing is clearly needed. Finally, microscopic examination of the fracture surfaces of each bar broken at 1300°C revealed that the origin of fracture in all specimens was due to surface machining (finishing) flaws.

The high temperature strength of GPS Si_3N_4 at 1400°C was measured by using poorly sintered material from billet #65. Although the average density of this billet was ~98% of the theoretical value, there were regions incompletely densified near the ends of the billet. Even though test bars machined from this billet exhibited "white spots" indicative of low density regions, it was nevertheless useful to measure the relative strength retention at 1400°C with probable low strength material. The average room temperature strength of 3 test bars (2.5 x 2.5 x 26 mm) in 3-pt bend using a span length of 1.6 cm) was, as expected, only 430 MNm^{-2}(62,270 psi). The average value of the short-term strength at 1400°C in air was 378 MNm^{-2}(54,800 psi). Although the absolute strengths were low because of the poor mechanical quality of sintered billet #65, it was gratifying to note that the short-term strength of GPS Si_3N_4 at 1400°C in air was ~88% of its room temperature strength. It is interesting that this same percentage of room temperature strength achieved at 1400°C has been previously observed for hot pressed Si_3N_4 of nearly the same composition but consisting of nearly a single phase microstructure.[16]

The main reason for the lack of more strength measurements at R.T. and elevated temperatures was that there were various furnace conditions that resulted in considerable difficulty in obtaining uniform density in the

larger, sintered billets. As previously mentioned, the initial green compacts weighed $\sim$15 g and had a length of $\sim$34 mm and diameter of $\sim$19 mm. The final sintered billets had occasionally a porous outer shell of variable thickness which completely surrounded part of the sintered sample near one end. A polished cross section made through the center of the sintered piece is illustrated in Fig. 21A. The porous region (white) in Fig. 21A was exposed to a low sintering temperature whereas the right edge of the sample experienced internal cracking due to a high sintering temperature where bloating was evident. This problem was clearly evidenced by color appearance and non-uniform shrinkage of the sintered compact and has been traced to a shorter hot zone in our rebuilt pressure furnace.

The length of the hot zone is determined by the resistance of the grafoil heating element in the vicinity of the hot zone as well as the rate of heat flow to the water-cooled ends of the furnace. Silicon carbide forms in the hot zone on the grafoil heater element due to the volatilization of Si and SiO vapors from the Si_3N_4 compositions during sintering. This SiC formation affects the resistance and, consequently, the localized temperature in the hot zone. The temperature gradient can be reduced significantly by increasing the amount of insulation to the maximum amount. In an attempt to overcome this occasional irritating problem, the long green compact was first sintered to its closed pore stage in 20 atm of N_2 gas, then the sample ends reversed in the hot zone, again sintering to hopefully close off all pores in the compact, and finally sintering in 70 atm of N_2 pressure to possibly drive the sintering process to completion. This attempt was unsuccessful as illustrated in Fig. 21B. Here, the final sintered sample exhibited extensive internal cracking, probably caused by non-uniform shrinkage stresses, which rendered the sample useless for making MOR test measurements.

B. Creep Resistance

The creep behavior of GPS Si_3N_4 was measured in air as a function of temperature, stress and post-sintering annealing for both short and long time experiments. Creep determinations were made on test bars machined from sintered billets #35, #38 and #65. The test bars nominally 2.5 mm x 2.5 mm x 2.6 cm long were loaded in a 3-pt bending mode using SiC fixtures. The configuration of test specimen, support and loading fixtures are shown in Fig. 22. These parts were located in a 15 cm x 15 cm x 15 cm box furnace equipped with super Kanthal 33 heating elements 15 cm long. The furnace was capable of operating in air at 1600°C.

Deflection of the test specimen was measured with a DC-operated LVDT (Linear Variable Differential Transformer) manufactured by Schaevity Engineering Model Number 050DC-D. This model LVDT operated with a sensitivity of about 80V/cm. When assembled and under test, the specimen was stressed by dead weight loading external to the furnace. The span of the specimen under load was ∿2.25 cm.

The creep strain data presented in Figs. 23 and 24 show that GPS Si_3N_4 exhibits excellent resistance to creep deformation at temperatures between 1300 and 1400°C in air. Fig. 23 shows that the steady-state creep rate at 1300°C and 1400°C are only 4.6 x 10^{-7} and 6.9 x $10^{-6}h^{-1}$, respectively, for an applied stress of 69 MNm^{-2}(10,000 psi). These creep rates are close in value to those measured for hot pressed β-Si_3N_4 containing small amounts of Be and O in solid solution.[16] However, the creep rate for GPS Si_3N_4 is about a factor of 100 lower than that measured for commercial NC-132 Si_3N_4 containing a Mg-additive. The creep data for NC-132 measured in compression by Seltzer[30] and some recent creep data obtained on sintered SiAlON[31] are also presented for comparison.
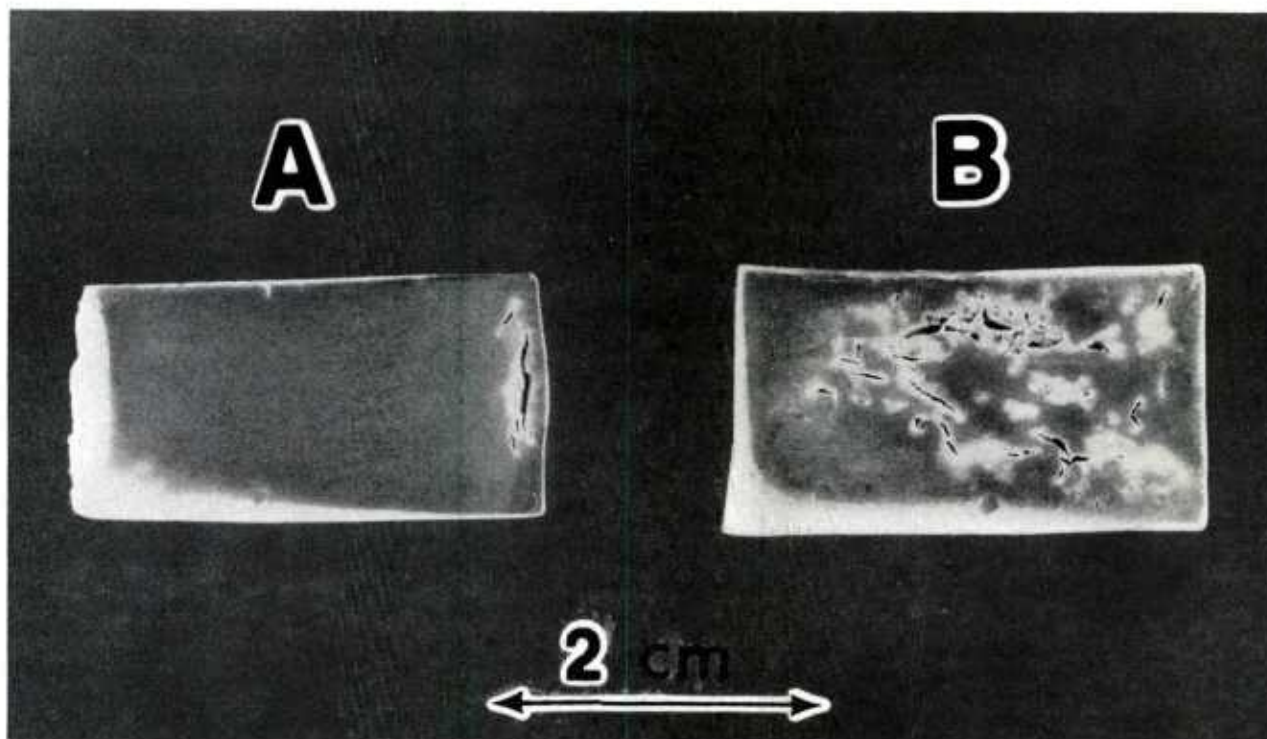
Figure 21. Porosity and crack development in large compacts of Si_3N_4 containing ~1 wt% Be and 3.5% O and sintered in a temperature gradient.

LOADING TRAIN

LOADING PIN

SPECIMEN
SUPPORT PINS

SiC SUPPORT TUBE

SiC INNER TUBE
TRANSMITTING
DEFLECTION
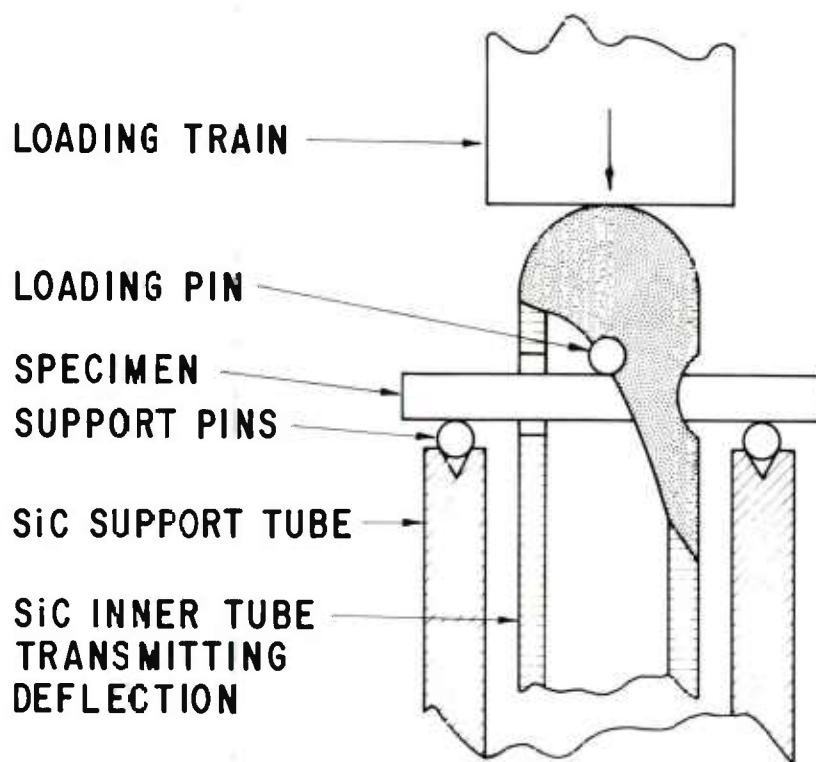
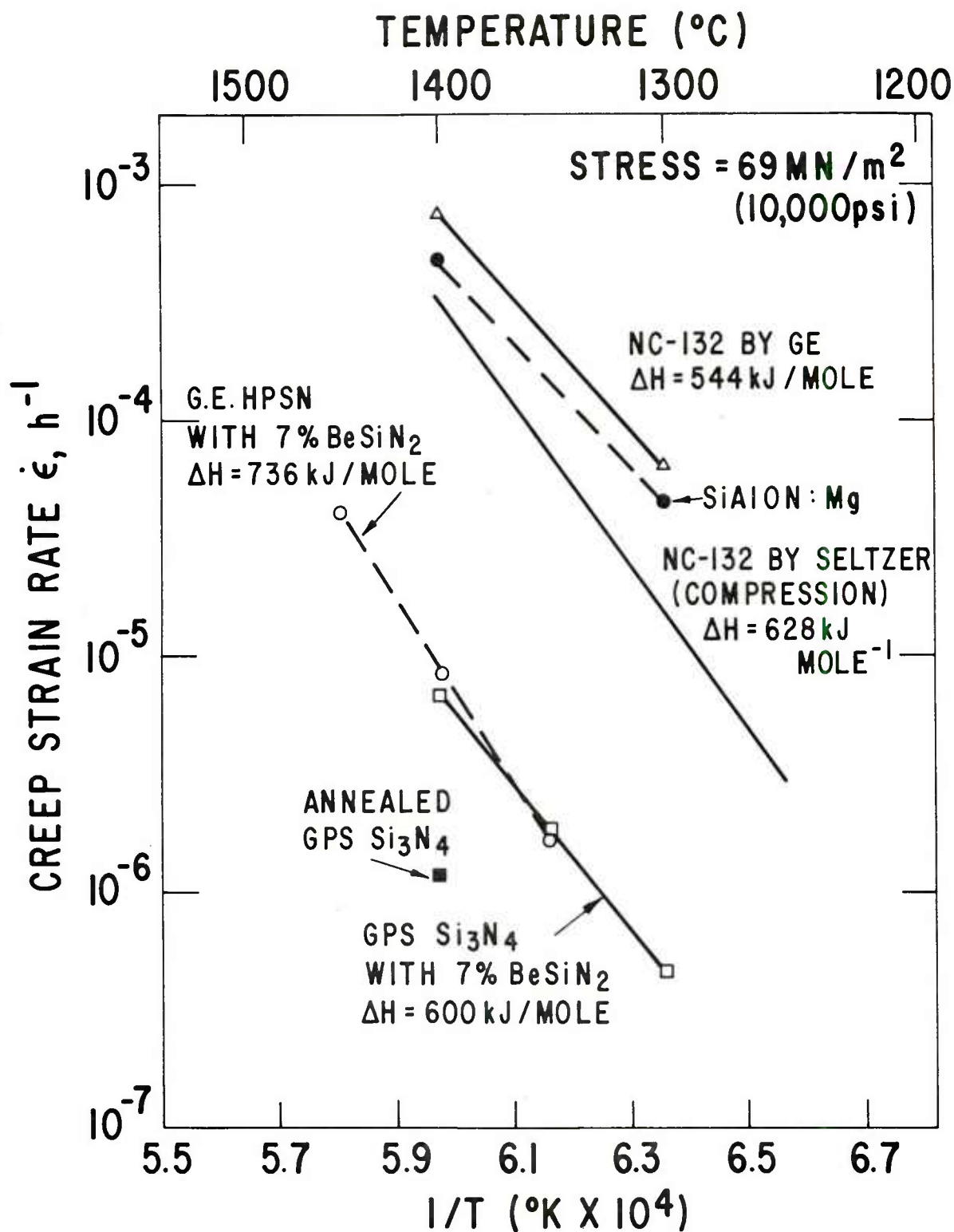Figure 22. Configuration of creep test specimen, supports and loading fixtures.

Figure 23. Steady state creep rate vs. 1/T for GPS Si₃N₄ and for hot pressed NC-132 Si₃N₄ used as a reference material. The creep data for several other compositions of Si₃N₄ are also plotted. SiAlON: Mg (ref.), NC-132 in compression (ref.) and G.E. HPSN with 7% BeSiN₂ (ref.).

61
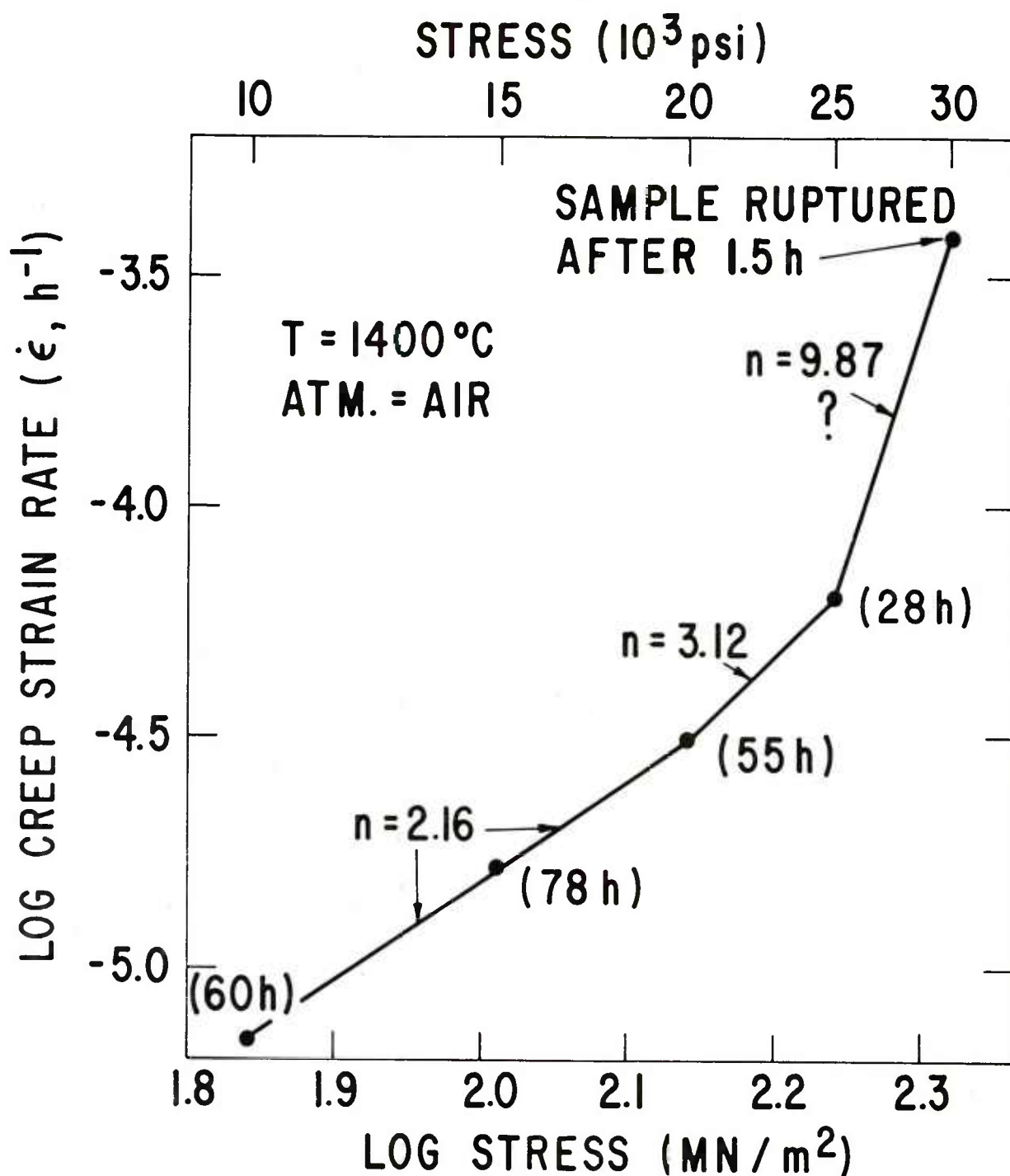
Figure 24. Log steady state creep rate vs. log stress for GPS Si$_3$N$_4$ at 1400°C in air. Numbers in parenthesis are the duration of the applied stress, and the n-values are those calculated for two levels of stress.

The steady state creep rate, $\dot{\varepsilon}$, is governed by the following empirical equation

$$\dot{\varepsilon} = A\sigma^n \exp(-\Delta H/RT) , \qquad (19)$$

where A is a constant dependent on microstructure, σ the applied stress, n the stress exponent, ΔH the enthalpy of activation and RT the thermal energy. From the data presented in Fig. 23, the ΔH value is not much different between hot pressed NC-132 (ΔH = 544 kJ/mole) and GPS Si_3N_4 (ΔH = 600 kJ/mole), suggesting that the presence of a residual glassy phase in both forms of Si_3N_4 may be responsible for a similar grain boundary sliding-diffusion model accompanied by other microstructural changes. The higher activation energy of 735 kJ/mole for GE-HPSN[16], containing 1 wt% Be and 3% O in solid solution, is probably related to it being a single-phase solid solution with virtually no glassy phase.

The steady-state creep rate as a function of stress at $1400^\circ C$ in air is shown on a log-log plot in Fig. 24. Again, very low creep rates of 10^{-5} to $10^{-4}h^{-1}$ are observed for maximum tensile stresses between 69 and 173 MNm^{-2}(10,000 and 25,000 psi). The numbers in parenthesis represent the number of hours that the test bar was in steady-state creep at the given stress level, and the stress exponent, n, is determined from the neighboring stress levels applied. Note that the stress exponent is determined to be ≈ 2.16 for applied stresses of 69, 104 and 137 MNm^{-2} but begins to increase to a value of 3.12 between stresses 138 and 173 MNm^{-2} (20,000 and 25,000 psi). Although the creep rate increased markedly between stresses of 173 and 207 MNm^{-2}, it is not sure that steady state creep was reached at a stress of 207 MNm^{-2}(30,000 psi) because of specimen rupture

after only 1.5 h. Therefore, the large n-value of ~9.9 is probably not meaningful. The total creep strain accumulated by this specimen before rupture was ~0.57%.

The effect of post-sintering annealing on the creep resistance of GPS Si_3N_4 was investigated for one creep bar made from billet #65. This bar was annealed at $1650°C$ for 16 h in one atm of N_2 gas to possibly crystallize some of the intergranular glassy phase. There was no weight change upon annealing, suggesting no change in the nominal composition of the test bar. X-ray diffraction analysis showed that the annealed bar contained an increased amount of Si_2N_2O which apparently crystallized from the glassy phase. The oxygen content of the as-sintered billet #65 was measured to be 2.89 wt% by neutron activation analysis. One creep result, plotted in Fig. 23 for this annealed GPS Si_3N_4, shows that the creep rate was reduced by a factor of 6 from $7 \times 10^{-6}h^{-1}$ to $1.2 \times 10^{-6}h^{-1}$ at $1400°C$ for an applied stress of $69 \ MNm^{-2}$. The steady state creep rate of this annealed bar was $5.2 \times 10^{-6}h^{-1}$ at a stress of $138 \ MNm^{-2}$ for 72 h.

A long term creep experiment was made with the same annealed bar of GPS Si_3N_4 after it was crept at $1400°C$ for 72 h in air. In this experiment the "annealed" bar was reheated to $1305°C$ and a stress of $207 \ MNm^{-2}$(30,000 psi) applied. This stress was maintained on the specimen for 300 h (12.5 days) in air without specimen rupture. The creep behavior followed steady-state conditions after about 20 h and resulted in a steady-state creep rate of 3.3 $\times 10^{-7}h^{-1}$ for a stress exponent equal to 2.13. After being stressed at 69 and $138 \ MNm^{-2}$ at $1400°C$ for ~100 h and stressed at $207 \ MNm^{-2}$ at $1305°C$ for 300 h, the total creep strain accumulated in the annealed bar of GPS Si_3N_4 was measured to be 0.078% by the LVDT measurements and 0.085% by physical measurement of sample curvature. An X-ray diffraction pattern of the annealed crept bar showed a primary phase of β-Si_3N_4 solid solution, trace of

Si_2N_2O (present from the annealing treatment) and α-SiO_2 (cristobalite). The α-SiO_2 formed primarily from oxidation of Si_3N_4 during the creep experiment at $1400^\circ C$ in air, but the oxide layer was very thin, as expected from oxidation kinetics at $1400^\circ C$ discussed in the following section.

Some microstructural evidence for identifying the creep mechanism in GPS Si_3N_4 is given in Figs. 25 and 26 for electron-transparent sections of the tensile and compression faces of creep bars near the center of each face. Figs. 25A and B shows that isolated intergranular cavitation is observed at 3-grain junctions where the glassy phase originally resides in the sintered product. In fact, the glassy phase surrounds both of the cavities, illustrated in Fig. 25, which formed in the annealed bar of GPS Si_3N_4 that was crept finally at $1305^\circ C$ for 300 h at a maximum tensile stress of 207 MNm^{-2}. Fig. 26 shows the extent of cavitation formed in the creep bar given the stepped stress treatment shown in Fig. 24 and which ruptured after 1.5 h at $1400^\circ C$ under a stress of 207 MNm^{-2}. Fig. 26A shows that the structure development in the tensile region of the crept bar is composed of not only isolated cavities formed at grain boundary triple points but also cavities that occupy grain faces and occasionally link-up to form large intergranular cracks. (Cavitation formation of this type has been recently observed in creep specimens of hot-pressed SiAlON ceramics[31]). It is interesting to note that isolated cavities also form at the 3-grain intersections on the <u>compression</u> surface of the creep bar, as shown in Fig. 26B. These microstructural observations of intergranular cavitation, grain boundary separation and microcrack extension in creep specimens having a stress exponent of ≈ 2.13 and very low absolute creep rates suggests that the mechanism of "steady state" creep in GPS Si_3N_4 involves grain boundary sliding accommodated by cavitation and grain boundary separation (controlled probably by diffusional creep).
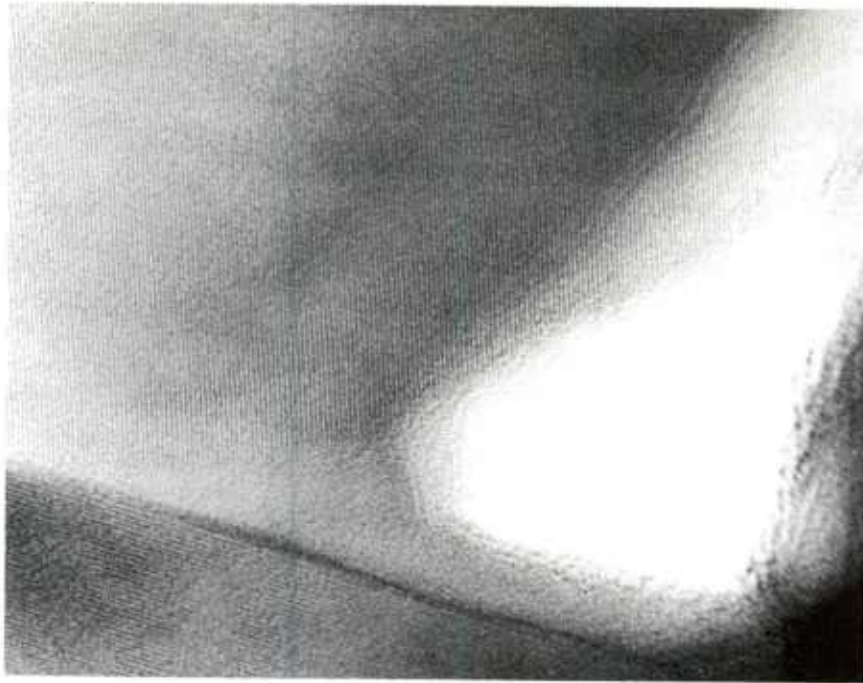
(a)
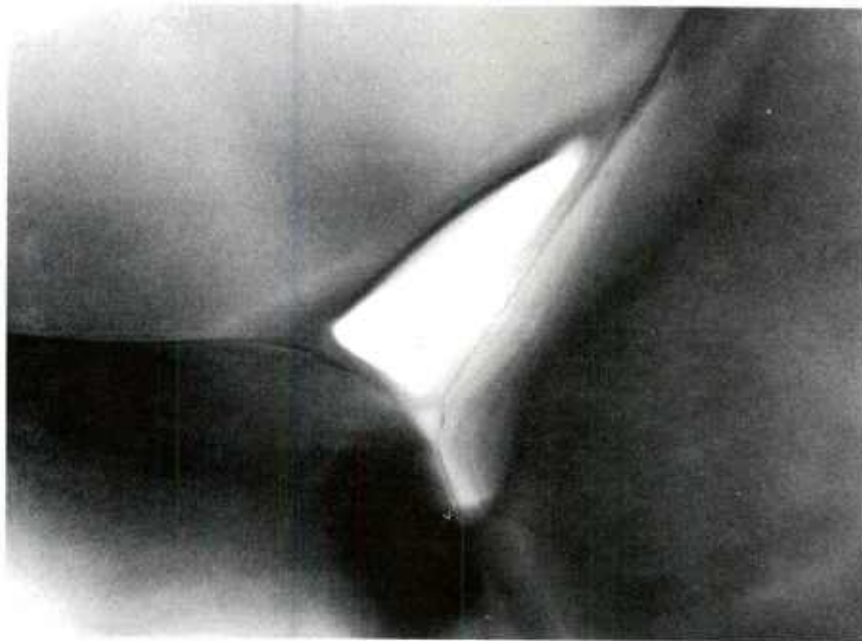
(b)

Figure 25. Internal cavitation formed in the glassy phase at triple-pt pockets between $-Si_3N_4$ grains near the maximum tensile stressed region of a crept specimen of GPS Si_3N_4 exposed to 207 MN/m^2 stress at 1305°C for 300 h in air. (A) Mag. = 8.6 x 10^{5}X and (B) Mag. = 1.25 x 10^{5}X.

(a)

(b)

Figure 26. (A) Link-up of intergranular cavities that cause grain boundary separation and crack growth in the tensile region of a creep specimen of GPS Si_3N_4 which ruptured at 1400°C after accumulating 0.57% strain. (TEM, mag. = 13,000X). (B) Isolated, triple-pt cavities located in the compression region of the same creep bar as in (A) (mag. = 13,000X).

C. Oxidation

The oxidation behavior of dense (>99%), GPS Si_3N_4 was investigated over the temperature range of 1000 to 1500°C in air or oxygen for times up to 300 h. Typically, bar-shaped samples were used and had surface areas between 1.5 and 5 cm^2 and weights between 0.2 and 2 grams.

The oxidation of clean test pieces of sintered Si_3N_4 finished with 320 grit diamond was performend in several Al_2O_3 tube furnaces. In one furnace Al_2O_3 tubes (55 cm x 2.5 cm) were first baked-out at 1700°C for 24 h to volatilize alkali impurties which may have spurious effects on the oxidation rate. The Si_3N_4 specimen was placed on a S.C setter which lay on either an Al_2O_3 or a zircon boat for oxidation temperatures at or below 1500°C. The assembly was inserted within 2 minutes into the hot furnace maintained at the desired temperature. Although in most cases the oxidaton atmosphere was oxygen flowing at ~5 cc/sec, there was little difference in oxidation rate when air was used. Specimens were periodically removed from the furnace and their weight measured on a Mettler H54 AR balance capable of measuring weight reproducibly to the nearest 2 x 10^{-5}g. The amount of oxidation was determined from weight gain measurements expected according to reaction(8). The parabolic rate constant (k_p) was determined by using the equation,

$$(\Delta W/A)^2 = k_p t, \tag{20}$$

where $\Delta W/A$ is the change in weight per unit area and t is the time. The oxidation results for gas pressure sintered Si_3N_4 are shown in Fig. 27. The kinetics of oxidation of one composition of GPS Si_3N_4 initially containing 1 wt% Be and 3.7 wt% O are represented by the curves obtained at 1400, 1450 and 1500°C. The fourth curve in Fig. 27 represents a set of data taken at 1400°C on a specimen oxidized in a "contaminated" atmosphere, i.e., the

68
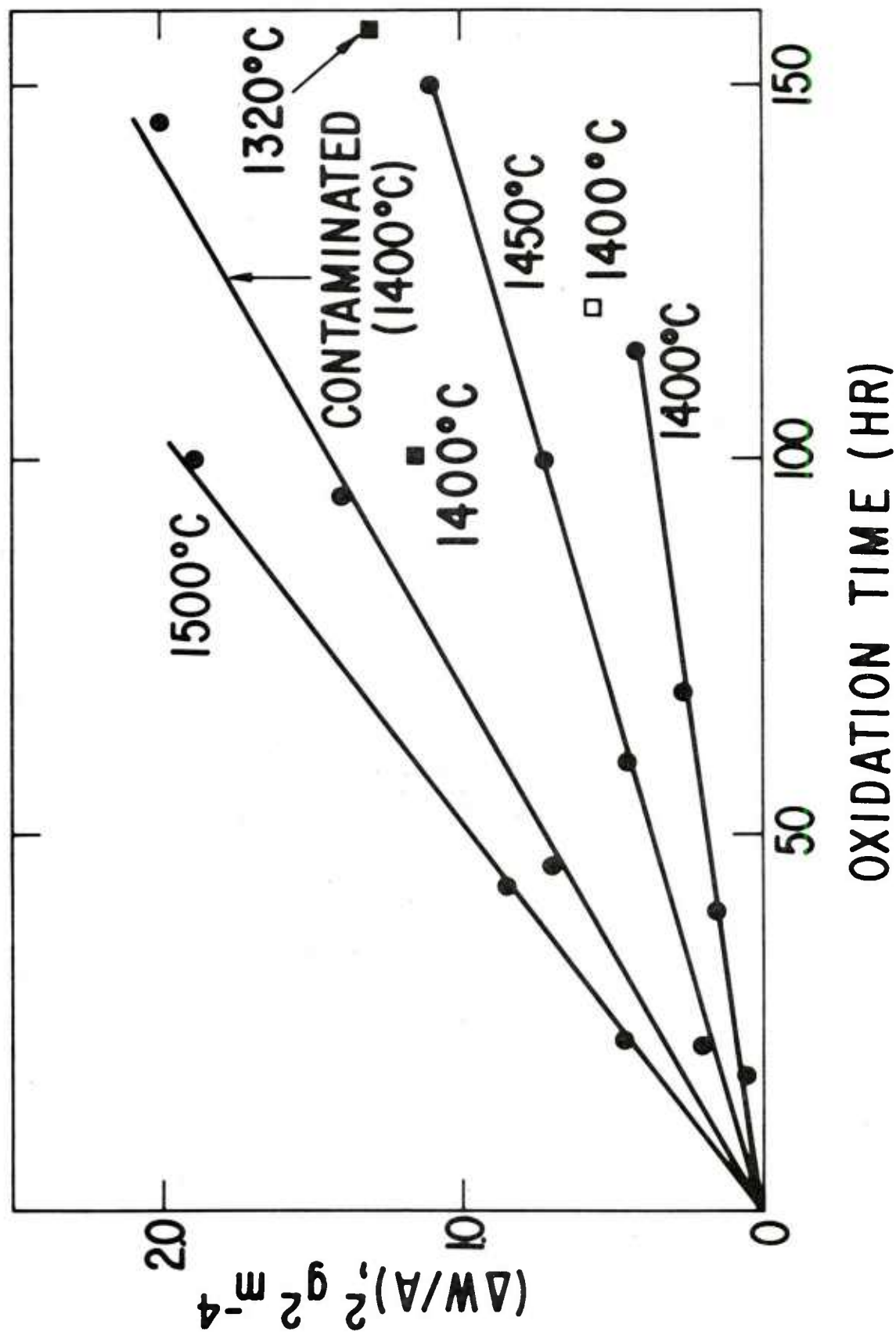
Figure 27. Kinetics of oxidation of GPS Si_3N_4 at temperatures between 1300 and 1500°C in air. Contamination from the furnace atmosphere typically increases the oxidation rate.

Al_2O_3 tube continued to evolve volatiles (probalby alkalis) which contaminated the surfaces of the Si_3N_4 specimen. In the latter case the parabolic rate constant at 1400°C for the contaminated specimen was 4 times higher than that of the uncontaminated one at the same temperature. These data, as well as the single data points (closed squares in Fig. 27) obtained at 1320 and 1400°C for oxidation experiments performed in other furnaces, show that for high oxidation-resistant GPS Si_3N_4 impurity contamination during oxidation may control the overall kinetics of the process. The open square in Fig. 27 shows that the oxidation behavior at 1400°C in oxygen is essentially reproducible in the same furnace even over a time period of 6 months.

The parabolic rate constants for oxidation of the "uncontaminated" sintered specimens at 1400, 1450 and 1500°C were 1.1×10^{-12}, 2.0×10^{-12} and 5.8×10^{-12} kg^2m^{-4}, s^{-1}, respectively. These oxidation rates are very low and comparable to those values found for hot pressed $-Si_{2.9}Be_{0.1}N_{3.8}O_{0.2}$. In fact, the oxidation rate of sintered Si_3N_4 is about 3 orders of magnitude lower than that for commercially hot pressed NC-132 Si_3N_4 oxidized in the same furnace at 1400°C.[23] The activation energy for oxidation of sintered Si_3N_4 was calculated from the slope of the plot of log k_p versus 1/T for the 3 data points. The activation energy was determined to be ≈ 418 kJ/mole (100 kcal/mole), a value higher than those values (375 kJ/mole[32] and 295 kJ/mole[33]) found for hot pressed Si_3N_4 containing 1% MgO.

An oxide scale formed on sintered Si_3N_4 between 1300 and 1500°C in O_2 and was composed of a fine network of microcracks associated with the $\beta-\alpha$ cristobalite transformation. X-ray diffraction revealed only the presence of α-cristobalite in the oxide scale. The oxide scale was thin and was coherently bonded to the Si_3N_4 substrate in all cases. Occasional white spots formed on the oxidized surfaces and were probably related to airborne particles (Al_2O_3, ?) in the furnace atmosphere.

A long oxidation run was also carried out at a relatively low temperature of 1000°C in order to determine if catastrophic oxidation, typical of some hot pressed forms of Y_2O_3-containing Si_3N_4 ceramics[34], occurred also in sintered Si_3N_4 containing small amounts of Be and O primarily in solid solution. After oxidation at 1000°C for 92 h in air, there was no detectable weight gain or oxidation. This information suggests that the oxidation resistance appears to be excellent over the temperature range of 1000-1500°C in oxidizing atmospheres.

D. Fracture Toughness

The fracture toughness, K_c, is the resistance of a material to fracture and is an important parameter affecting the strength of brittle ceramics. Although little K_c-data has been obtained on dense, polycrystalline ceramics, it has been reasonably well demonstrated that the K_c of hot-pressed Si_3N_4 depends on chemical composition and microstructure.[24,35-38]

The K_c-values of two sintered samples, one made from processed Sylvania powder and the other made from processed Starck Si_3N_4 powder, were measured by the microhardness indentation technique[39] in a Vicker's test using flat, polished samples. In addition, the fracture toughness of NC-132 hot pressed Si_3N_4 was measured by the same method and served as a reference material. The use of a 500-750 g load resulted in sharp indentor impressions with single extension cracks radiating outward from the impression corners in NC-132 material. The value measured for fracture toughness was 3.7 $MNm^{-3/2}$ for NC-132 Si_3N_4. The corresponding Vicker's hardness number for NC-132 Si_3N_4 was 1800 kg/mm^2 for a 500 g load.

The indentor impressions for the sintered Si_3N_4 samples were not clearly defined in many cases. A bar of sintered billet #35, which had a

modulus of rupture of 642 MN/m^2 (93,000 psi) and a density of 99.1%, typically exhibited indentor impressions characterized by more than 1 crack emanating from each impression corner regardless of the load between 750 and 250 g. However, several impressions were made with 250 and 350 g loads that exhibited single extension cracks. The fracture toughness determined from these impressions was 2.9 MN/m$^{-3/2}$, or about 22% lower than that measured for NC-132 Si$_3$N$_4$. The hardness number was about 1650 kg/mm^2 for a load of 500 g.

The fracture toughness of sintered Starck material, containing 0.5 wt% Be and $\sim$2.5 wt% O, was found to be 3.1 MN/m$^{-3/2}$. The sample contained approximately 3% porosity and, consequently, the hardness number was only 1450 kg/mm^2 with a 500 g load. This specimen also exhibited a few cracks originating from the edges as well as from the corners of the indentor impressions.

E. Thermal Expansion

The thermal expansion behavior of 99.1% dense, GPS Si$_3$N$_4$ cut from billet #55, was measured from room temperature to 1000°C in air at a heating and cooling rate of $\sim$4°C/min in a fused silica dilatometer. The dimensional changes during heating and cooling were very smooth with little hysteresis effects. The thermal expansion coefficient of GPS Si$_3$N$_4$ was measured as 2.8 x 10^{-6} °C^{-1}.

IX. SINTERING COMPLEX SHAPES FORMED BY SLIP CASTING

One of the main objectives of this program was to demonstrate that dense, complex shapes of Si$_3$N$_4$ can be produced by the sintering process. This achievement has been realized during this contracting period by sintering slip-cast (modified T-700) blades to densities of 98% relative density.

Slip cast blades (3 cm long x 1.8 cm wide) were made from a processed SN502-74 Si_3N_4 powder of high cation purity but containing 7 wt% $BeSiN_2$ and about 3.5-3.6 wt% oxygen as densification aids. The $BeSiN_2$ is added during the comminution step of the Si_3N_4 powder whereas the oxygen content is controlled by oxidation of the final green part. The starting Si_3N_4 powder had a specific surface are of $\approx 8.8\ m^2$ g and an initial O-content of 1.34 wt%.

Slips having a pH~10 and solids content of 27, 32, 38 and 43 volume % were prepared by using water as the liquid medium, tetramethylammonium hydroxide as the particle deflocculating agent and about 0.2 wt% urac resin to improve green strength of the slip-cast part. In all cases the Si_3N_4 slips tended to exhibit some degree of thixotropic behavior. High concentrations of urac resin near 1 wt% resulted in stronger green bodies but more porous sintered articles. Slip cast parts having a solids content of 27 and 32 vol. % were easily removed from the plaster-of-paris molds whereas parts made from the suspension containing 43 vol. % solids stuck to the molds in every case. The use of 1/2 wt% Na-alginate solution to improve mold release still proved unsuccessful. The green blades of the highest green density (~57% of theoretical), which could be removed from the molds without cracking with reasonable success, were produced from the suspension containing ~38% solids. All dried, "green" blades contains some small tears and surface cracks especially in the dovetail and platform regions of the blade. The elimination of these small cracks might be achieved through optimization of the casting time and slip rheology.

The green blades were then oxidized at 650°C in air for 1 h to remove the moisture and urac resin, and then oxidized at 1045°C for ~30 min to increase the oxygen content of the blades from 1.34 to 3.5-3.6 wt%. Each oxidized green blade was then placed in a BN crucible and sintered by the

established GPS process using a heating rate of $\sim 10^{\circ}$C/min and a peak sintering temperature of 2000°C in 20 atm of N_2 for 15 min.

Green blades having low relative green densities of 40 to 45% and high concentrations of urac resin typically sintered to 90-93% relative density but underwent large weight losses of 4-7%. Some open porosity was usually detected in these sintered blades. Observation of sintered blades under a low power optical microscope reveals that a series of short small cracks (50 microns) exist in the dovetail region of both samples due to poor mold release of the green blade. In addition, there were 1 or 2 small microcracks located under the platform region. These defects, in our estimation, can be traced back to the nature and improper formulation of the initial slip-cast suspension. Furthermore, the larger weight losses of 4-7 wt% observed for sintered slip-cast parts, as compared to 1-2 wt% for die-pressed parts, signifies that the sintered parts have large pores and some surface cracks which act as sites for continual thermal decomposition and weight loss.

Three green blades that had high relative green densities of ~ 55-57% and lower (0.2 wt%) amounts of urac resin were sintered to relative densities of 96, 97 and 98%. Linear shrinkage and weight loss for these blades were about 19% and 2%, respectively. The degree of shape and dimensional changes in going from the green blade to the sintered blade is illustrated in Fig. 28. The sintered blades undergo nearly uniform shrinkage and some shape distortion of the airfoil section. Although no microscopic cracks are observed in the airfoil portion, there are a few thin (25-50 microns) cracks as long as 0.5 mm long in the platform/dovetail region.

One of the sintered blades having an average relative density of 96% was sectioned parallel to the long axis of the blade and polished. Microscopic examination of this blade showed that there was more porosity in the central

portion of the section than elsewhere. Fig. 29A shows that a uniform microstructure occurs near the external surface of the sintered blade in the platform region. The microstructure shown in Fig. 29B is typical of that found throughout the cross section of the blade except in the direct central region. Here, there is a small volume fraction of pores having sizes as large as 10 microns. On the other hand, a considerable amount of porosity is found in the central portion of the blade and illustrated in Fig.29C. Clearly, the properties of the Si_3N_4 slip need to be optimized and understood before this problem of nonuniform distribution of porosity can be solved in GPS Si_3N_4 blades.
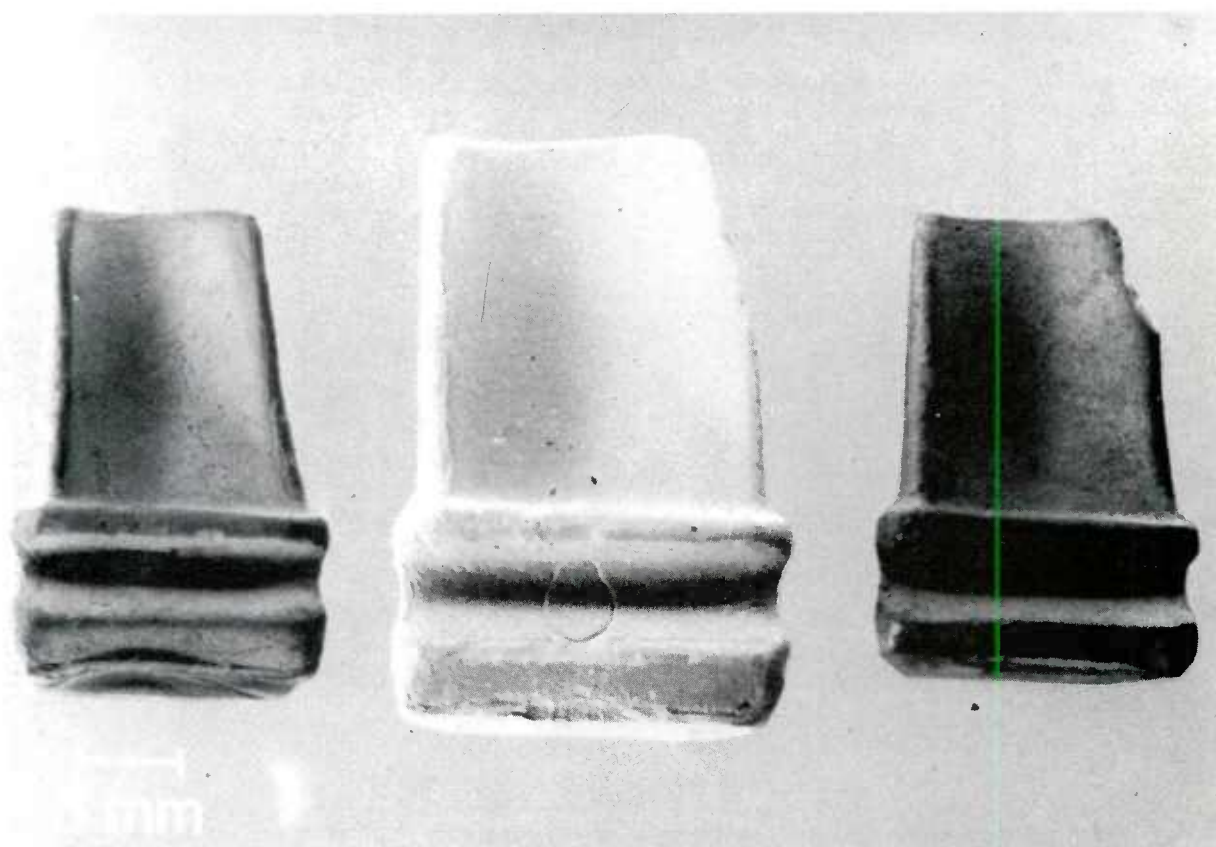
Figure 28. Slip-cast blades of the composition Si_3N_4 + 7 wt% $BeSiN_2$ + 3.5 wt% O showing a green blade (middle) and two blades (left and right) given the GPS process.
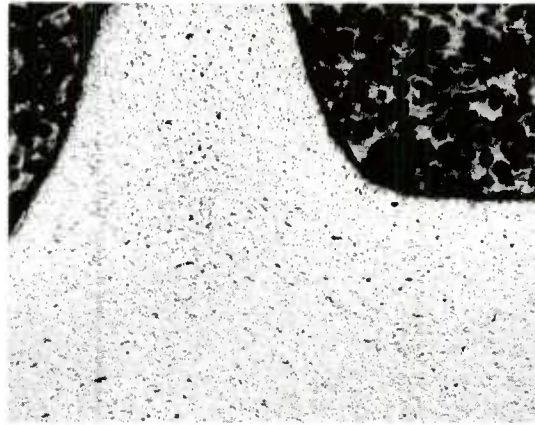
(a)
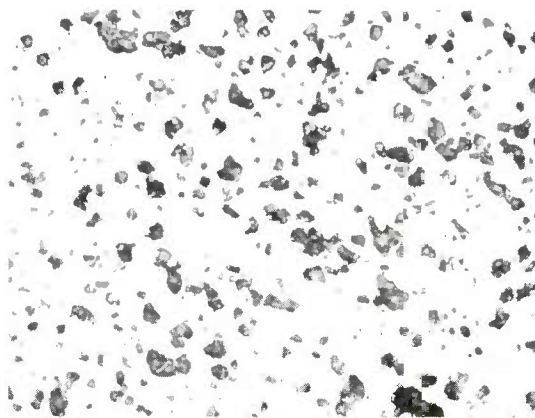
(b)

(c)

Figure 29. Microstructures of a blade having
an average relative density of 96%.
(A) platform region, Mag. = 20X,
(B) typical microstructure
throughout the majority of the
sintered blade, Mag. = 500X, and
(C) high volume fraction of porosity
in the direct central region of the air-
foil section, Mag. = 500X.

REFERENCES

1. A.E. Gorum, J.J. Burke, E.M. Lenoe, and R.N Katz, in Proceedings of the NATO-CCMS Symposium on Low Pollution Power Systems Development, Dusseldorf, November 1974.

2. S. Prochazka, in Ceramics for High Performance Applications, edit. by J.J. Burke, A.E. Gorum and R.N. Katz, Brook Hill Pub. Co., Chestnut Hill, Mass., 1974.

3. G.R. Terwilliger, J. Am. Ceram. Soc., 57 48 (1974).

4. G.R. Terwilliger and F.F. Lange, J. Mat. Sci., 10 1169 (1975).

5. M. Mitomo, M. Tsutsumi, E. Bannai and T. Tanaka, J. Am. Ceram. Soc., 55 313 (1976).

6. M. Mitomo, J. Mat. Sci., 11 1103 (1976).

7. D.J. Rowcliffe and P.J. Jorgensen, SRI International Final Tech. Rept., NSF Grant No. AER75-14896, Dec. 1977.

8. R.E. Loehman and D.J. Rowcliffe, J. Am. Ceram. Soc., 63 144 (1980).

9. R.J. Lumby, B. North and A.J. Taylor, in Nitrogen Ceramics, edit. by F.L. Riley, p. 393 Noordhoff Int. Pub., Reading, Mass., 1977.

10. L.J. Gauckler, S. Boskovic and G. Petzow, ibid., p.405.

11. R.R. Wills, R.W. Stewart and J.M. Wimmer, J. Am. Ceram. Soc., 60 64 (1977).

12. I. Oda, M. Kaneno and N. Yamamoto, in Nitrogen Ceramics, edit. by F.L. Riley, p. 359, Noordhoff Int. Pub., Reading, Mass., 1977.

13. H.F. Priest, G.L. Priest and G.E. Gazza, J. Am. Ceram. Soc., 60 81 (1977).

14. J.A. Palm and C. Greskovich, GE Rept. SRD-78-076 under NASC Contract N00019-77-C-0259, July 1978.

15. C. Greskovich, J. Mat. Sci., 14 2427 (1979).

16. J.A. Palm and C. Greskovich, Am. Ceram. Soc. Bull., 59 447 (1980).

17. I.C. Huseby, H.L. Lukas and G. Petzow, J. Am. Ceram. Soc., $\underline{58}$ 377 (1975).

18. G. Hetherington, K.H. Jack and J.C. Kennedy, Phys. Chem. Glasses, $\underline{5}$ 130 (1964).

19. S. Prochazka and C. Greskovich, Final Technical Rept. No. AMMRC TR 78-32, July 1978.

20. C. Greskovich, J.H. Rosolowski and S. Prochazka, ARPA Final Technical Report, G.E. Report No. SRD-75-084, 1975.

21. C. Greskovich and J.R. Rosolowski, J. Am. Ceram. Soc., $\underline{59}$ 336 (1976).

22. C. Greskovich, S. Prochazka and J.H. Rosolowski, in Nitrogen Ceramics edit. by F.L. Riley, p. 351, Noordhoff Int. Pub., Reading, Mass. 1977.

23. S. Prochazka and C. Greskovich, in Proc. of the International Symposium on Factors in Densification and Sintering of Oxide and Non-oxide Ceramics, edit. by S. Sōmiza and S. Saito, p. 489, Gakujutsu Bunken Fukyu-kai publisher, Japan, 1978.

24. F.F. Lange, J. Am. Ceram. Soc., $\underline{56}$ 518 (1973).

25. JANAF Thermochemical Tables, 2nd Edit., D.R. Stull and H. Prophet, NSRDS-NBS 37, U.S. Government Printing Office, Washington, D.C., 1971.

26. H.D. Batha and E.D. Whitney, J. Am. Ceram. Soc., $\underline{56}$ 365 (1973).

27. D.R. Messier and G.E. Gazza, ibid., $\underline{58}$ 538 (1975).

28. K.H. Jack, Trans. J. Brit. Ceram. Soc., $\underline{72}$ 376 (1972).

29. R.A. Morgan and F.A. Hummel, J. Am. Ceram. Soc., $\underline{32}$ 250 (1949).

30. M.S. Seltzer, Am. Ceram. Soc. Bull., $\underline{56}$ 418 (1977).

31. B.S.B. Karunaratne and M.H. Lewis, J. Mat. Sci., $\underline{15}$ 449 (1980).

32. S.C. Singhal, ibid., $\underline{11}$ 500 (1976).

33. W.C. Tripp and H.C. Graham, J. Am. Ceram. Soc., $\underline{59}$ 399 (1976).

34. H. Knoch and G.E. Gazza, ibid., $\underline{62}$ 634 (1979).

35. F.F. Lange, ibid., $\underline{56}$ 445 (1973).

36. R.W. Rise and W.J. McDonough, ibid., $\underline{58}$ 264 (1975).

37. F.F. Lange, ibid., $\underline{62}$ 428 (1979).

38. G. Himsolt, H. Knock, H. Huebner and F.W. Kleinlein, ibid., $\underline{62}$ 29 (1979).

39. A.G. Evans and E.A. Charles, ibid., $\underline{59}$ 371 (1976).

No. of Copies	To	No. of Copies	To
	Office of the Under Secretary of Defense for Research and Engineering, The Pentagon, Washington, D.C. 2D3D1		Director, U.S. Army Ballistic Research Laboratory, Aberdeen Proving Ground, Maryland 21D05
1	ATTN: Mr. J. Persh	1	ATTN: DRDAR-TSB-S (STINFO)
1	Dr. G. Gamota		
			Commander, U.S. Army Test and Evaluation Command, Aberdeen Proving Ground, Maryland 21DD5
12	Commander, Defense Technical Information Center, Cameron Station, Building 5, 501D Duke Street Alexandria, Virginia 22314	1	ATTN: DRSTE-ME
			Commander, U.S. Army Foreign Science and Technology Center, 220 7th Street, N.E., Charlottesville, Virginia 22901
1	National Technical Information Service, 52B5 Port Royal Road, Springfield, Virginia 22161	1	ATTN: Military Tech, Mr. W. Marley
			Commander, Watervliet Arsenal, Watervliet, New York 12189
	Director, Defense Advanced Research Projects Agency, 1400 Wilson Boulevard, Arlington, Virginia 22209	1	ATTN: Dr. T. Davidson
1	ATTN: Dr. A. Bement		Director Eustis Directorate, U.S. Army Mobility Research
1	Dr. Van Reuth		and Development Laboratory, Fort Eustis, Virginia 236D4
		1	ATTN: Mr. J. Robinson, SAVDL-E-MOS (AVRADCOM)
	Battelle Columbus Laboratories, Metals and Ceramics Information Center, 505 King Avenue, Columbus, Ohio 43201	1	Mr. C. Walker
1	ATTN: Mr. Winston Duckworth		Chief of Naval Research, Arlington, Virginia 22217
1	Dr. D. Niesz	1	ATTN: Code 471
		1	Dr. A. Diness
	Deputy Chief of Staff, Research, Development, and Acquisition, Headquarters, Department of the Army, Washington, D.C. 20310	1	Dr. R. Pohanka
1	ATTN: DAMA-ARZ		Naval Research Laboratory, Washington, D.C. 20375
1	DAMA-CSS, Dr. J. Bryant	1	ATTN: Dr. J. M. Krafft - Code 5B30
		1	Mr. R. Rice
	Commander, U.S. Army Medical Research and Development Command, Fort Detrick, Frederick, Maryland 21701		Headquarters, Naval Air Systems Command, Washington, D.C. 2D36D
1	ATTN: SGRD-SI, Mr. Lawrence L. Ware, Jr.	1	ATTN: Code 5203
		1	Code MAT-042M
	Commander, Army Research Office, P.O. Box 12211, Research Triangle Park, North Carolina 27709	1	Mr. I. Machlin
1	ATTN: Information Processing Office		Commander, Naval Weapons Center, China Lake, California 93555
1	Dr. G. Mayer	1	ATTN: Mr. F. Markarian
1	Dr. J. Hurt		
			Commander, U.S. Air Force of Scientific Research,
	Commander, U.S. Army Materiel Development and Readiness Command, 5001 Eisenhower Avenue, Alexandria, Virginia 22333		Building 410, Bolling Air Force Base, Washington, D.C. 20332
1	ATTN: DRCOMO-ST	1	ATTN: MAJ W. Simmons
1	DRCLDC		Commander, U.S. Air Force Materials Laboratory, Wright-Patterson Air Force Base, Ohio 45433
	Commander, Harry Diamond Laboratories, 2800 Powder Mill Road, Adelphi, Maryland 207B3	1	ATTN: Dr. N. Tallan
1	ATTN: Mr. A. Benderly	1	Dr. H. Graham
1	Technical Information Office	1	Dr. R. Ruh
1	DELHD-RAE	1	Mr. K. S. Mazdiyasni
		1	Aero Propulsion Labs, Mr. R. Marsh
	Commander, U.S. Army Missile Command, Redstone Arsenal, Alabama 35B09		National Aeronautics and Space Administration, Washington, D.C. 20546
1	ATTN: Mr. P. Ormsby	1	ATTN: Mr. G. C. Deutsch - Code RW
1	Technical Library	1	Mr. J. Gangler
		1	AFSS-AD, Office of Scientific and Technical Information
	Commander, U.S. Army Aviation Research and Development Command, 4300 Goodfellow Boulevard, St. Louis, Missouri 63120		National Aeronautics and Space Administration, Lewis Research Center, 21000 Brookpark Road, Cleveland, Ohio 44135
1	ATTN: DRDAV-EXT	1	ATTN: J. Accurio, USAMRDL
1	DRDAV-QE	1	Dr. H. B. Probst, MS 49-1
		1	Dr. R. Ashbrook
	Commander, U.S. Army Tank-Automotive Research and Development Command, Warren, Michigan 4B090	1	Dr. S. Dutta
1	ATTN: Dr. W. Bryzik	1	Mr. C. Blankenship
1	Mr. E. Hamperian		National Aeronautics and Space Administration, Langley Research Center, Hampton, Virginia 23665
1	D. Rose	1	ATTN: Mr. J. Buckley, Mail Stop 3B7
1	DRDTA-RKA, Dr. J. Chevalier		
1	DRDTA-UL, Technical Library		Department of Energy, Division of Transportation, 2D Massachusetts Avenue, N.W., Washington, D.C. 20545
	Commander, U.S. Army Armament Research and Development Command, Dover, New Jersey 07B01	1	ATTN: Mr. George Thur (TEC)
1	ATTN: Dr. G. Vezzoli	1	Mr. Robert Schulz (TEC)
1	Technical Library	1	Mr. John Neal (CLNRT)
		1	Mr. Steve Wander (Fossil Fuels)
	Commander, U.S. Army Armament Materiel Readiness Command, Rock Island, Illinois 61299		Department of Transportation, 400 Seventh Street, S.W., Washington, D.C. 2059D
1	ATTN: Technical Library	1	ATTN: Mr. M. Lauriente
	Commander, Aberdeen Proving Ground, Maryland 21DD5		National Bureau of Standards, Washington, D.C. 20234
1	ATTN: DRDAR-CLB-PS, Mr. J. Vervier	1	ATTN: Dr. S. Wiederhorn
	Commander, U.S. Army Mobility Equipment Research and Development Command, Fort Belvoir, Virginia 22060		
1	ATTN: DRDME-EM, Mr. W. McGovern		
1	DRDME-V, Mr. E. York		

AD

Army Materials and Mechanics Research Center,
Watertown, Massachusetts 02172
DEVELOPMENT OF HIGH PERFORMANCE SINTERED Si₃N₄
Charles D. Greskovich and John A. Palm
General Electric Company
Corporate Research and Development
Schenectady, New York 12301

Technical Report AMMRC TR 80-46, September 1980, 29 pp -
illus - tables, Contract DAAG46-78-C-0058
Final Report, September 1978 to April 1980

Key Words

Gas Pressure Sintering
Silicon Nitride
High Temperature Properties

A gas pressure sintering (GPS) process has been developed to produce Si₃N₄, containing 0.5-1.0 wt% Be and 2.5-3.7 wt% 0, with >99% relative density. The modulus of rupture of GPS Si₃N₄ at 1300 °C was 553 MNm⁻² (80,200 psi), representing 93% of its room temperature strength. The creep and oxidation resistances were outstanding and evidenced by creep rates of 4.6 × 10⁻⁷ and 6.9 × 10⁻⁷h⁻¹ at a stress of 69 MNm⁻² (10,000 psi) at 1300 and 1400 °C in air, respectively, and parabolic oxidation rates of 1 × 10⁻¹² and 6 × 10⁻¹²kg² m⁻⁴s⁻¹ at temperatures between 1300 and 1500 °C in air. GPS Si₃N₄ survived a long term creep experiment of 207 MNm⁻² (30,000 psi) stress for 300 h at 1305 ° in air. A post sintering anneal increased the creep resistance of GPS Si₃N₄ by a factor of 6. The fracture toughness at room temperature and thermal expansion coefficient between R.T. and 1000 °C were 2.9 MNm⁻³/² and 2.8 × 10⁻⁶°C⁻¹, respectively.

The GPS process was successful in producing high density (98%), small blades of sintered Si₃N₄. Although problems with nonuniform porosity and surface microcracks were observed for the sintered blades, these problems are not intrinsic to the GPS process.